Indentation of adhesive beams

V.S. Punati [a,b,*], I. Sharma [a,b], P. Wahi [a,b]

[a] *Mechanics & Applied Mathematics Group, India*
[b] *Department of Mechanical Engineering, Indian Institute of Technology Kanpur, Kanpur, Uttar Pradesh, 208016, India*

A B S T R A C T

We investigate the contact of a rigid cylindrical punch with an adhesive beam mounted on flexible end supports. Adhesion is modelled through an adhesive zone model. The resulting Fredholm integral equation of the first kind is solved by a Galerkin projection method in terms of Chebyshev polynomials. Results are reported for several combinations of adhesive strengths, beam thickness, and support flexibilities characterized through torsional and vertical translational spring stiffnesses. Special attention is paid to the important extreme cases of clamped and simply supported beams. The popular Johnson–Kendall–Roberts (JKR) model for adhesion is obtained as a limit of the adhesive zone model. Finally, we compare our predictions with preliminary experiments and also demonstrate the utility of our approach in modeling complex structural adhesives.

© 2018 Elsevier Ltd. All rights reserved.

1. Introduction

Research in patterned adhesives is often motivated by the structures of natural adhesives, such as those present in the feet of gekkos; see e.g. Hiller (1976), and Arul and Ghatak (2008). In conventional adhesives, such as thin, sticky tapes, only the top and bottom surfaces are active. However, multiple surfaces may be activated with appropriate patterning. With more surfaces participating in the adhesion process the adhesives show increased hysteresis and, so, better performance. One example of a patterned adhesive is the structural adhesive shown in Fig. 1(a), which was developed by Arul and Ghatak (2008). Fig. 1(b) shows a possible mechanical model of the structural adhesive of Fig. 1(a) that utilizes several interacting adhesive beams. This motivates the goal of this paper, which is to investigate the adhesive contact of a beam; see Fig. 2(a).

Contact with a half-space has been well studied over the past century, and we refer the reader to Alexandrov and Pozharskii (2001), and also the texts of Galin and Gladwell (2008), Gladwell (1980), Johnson (1985) and Hills et al. (1993). At the same time, the contact of thin layers is an active area of research in view of applications to electronics and computer industry; see, e.g. Barthel and Perriot (2007), and Dalmeya et al. (2012). In contrast, the indentation of beams is much less studied.

Seeking the solution to the indentation of a beam through a strength-of-materials approach overlooks the local contact mechanics. To probe the latter, it is necessary to formulate an elasticity problem with appropriate boundary conditions. This is typically a complex problem, and has prompted some alternate approaches to adhesion*less* contact, as discussed in the next paragraph. To the best of our knowledge there is *no* available work on the adhesive contact of beams.

Two-dimensional adhesionless indentation of a beam has been studied in the past by Keer and Silva (1970), Keer and Miller (1983), Keer and Schonberg (1986), Sankar and Sun (1983), Sun and Sankar (1985), and Kim et al. (2014). Keer and Miller (1983) modeled the beam as a linear elastic layer of infinite extent with frictionless bottom and top surfaces. First, the elasticity problem was solved through Fourier transforms, see e.g. Sneddon (1995, p. 395–414). Then, employing the Hankel transform (Gladwell, 1980, p. 213) for the pressure distribution, and asymptotically matching the far-field displacements with those obtained from Euler-Bernoulli beam theory, a Fredholm integral equation of the second kind was obtained. This equation was solved numerically.

Sankar and Sun (1983) employed Fourier series in their investigation of adhesionless contact with beams of finite length. Their results were in good agreement with those of Keer and Miller (1983). Recently, Kim et al. (2014) studied beam indentation through asymptotics. Finite element (FE) simulations were also carried out. The contact parameters, i.e. contact area and the total load acting on the punch, obtained through asymptotics, matched results of FE simulations well. In all these studies, the interaction of the beam with the punch is non-adhesive. However, extending these methods to adhesive beams is difficult due to the presence of several iterated integral transforms.

* Corresponding author: .
  E-mail address: punati@iitk.ac.in (V.S. Punati).
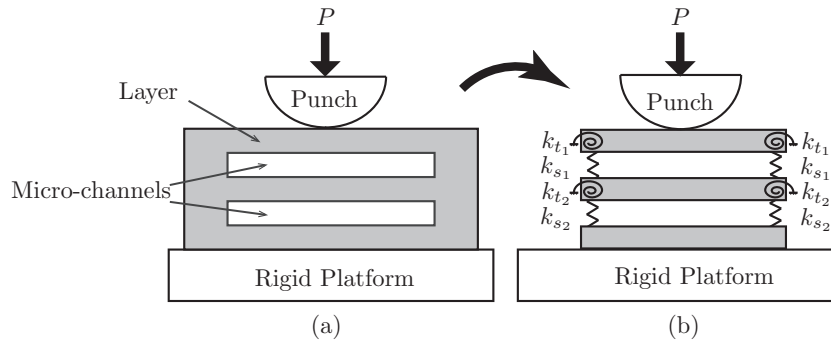
Fig. 1. (a) Structural adhesive designed by Arul and Ghatak (2008). (b) Mechanical model of the structural adhesive in (a) employing an interconnected stack of adhesive beams. The rigidity of the vertical walls is modeled through torsional (stiffness k_t) and vertical translational (stiffness k_s) springs, as shown. The system is indented by a rigid punch, pressed down by the force P.
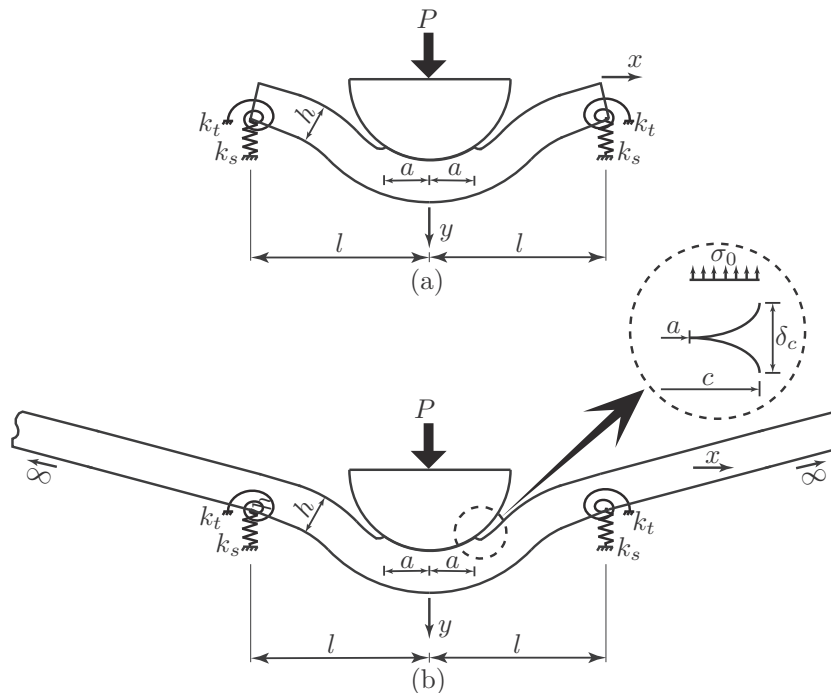
Fig. 2. (a) Indentation by a rigid cylindrical punch of an adhesive beam resting upon flexible supports. The flexible supports are modeled through torsional and vertical translational springs with stiffnesses k_t and k_s, respectively. (b) Mathematical model of the indentation process shown in (a). The inset shows details of the adhesive zone active near the contact edges; see text for details. The vertical deflection is exaggerated for ease of representation.

This paper is organized as follows. We start by formulating a mathematical model for the adhesive contact of the beam shown in Fig. 2(a). We will obtain a Fredholm integral equation of the first kind that relates the contact pressure distribution with the vertical displacement in the contact patch. Relevant conditions at the edge of the contact zone will also be derived. This integral equation is then solved numerically employing Galerkin projections in terms of Chebyshev polynomials. Theoretical results are compared with our own FE simulations whenever possible. We then explore the effect of various parameters in the problem, viz. flexibility of end supports, strength of adhesion, the beam's geometry, etc. We close with a comparison with preliminary experimental results, and an application of our solution to complex structural adhesives, such as the one shown in Fig. 1(a).

2. Mathematical model

We begin by extending the beam of Fig. 2(a) beyond the supports to infinity, as shown in Fig. 2(b). The extension is done in a manner consistent with the kinematic and kinetic constraints im-

posed by the supports. Thus, the beam is extended linearly along its slope at the supports. The beam may now be thought of as a linear elastic layer of infinite length with thickness h. The beam is isotropic and homogeneous, with Young's modulus E and Poisson's ratio ν. The top and bottom surfaces of the beam are frictionless.

During indentation, a normal traction distribution $-P_c(x)$ acts on the top surface.[1] At this time, the vertical displacement of the bottom surface is $v_b(x)$, which is typically *not* known. When the contact area is less than the beam's thickness, we assume that $v_b(x)$ may be approximated[2] by the displacement obtained from Euler-Bernoulli beam theory when a point load of magnitude P acts at the center of the top surface, as depicted in Fig. A.18. The details

---

[1] The negative sign is introduced in order to report compressive pressure during contact as positive.

[2] Punati (2017) presents an exact analysis predicated on the solution of a system of dual integral equations in which $v_b(x)$ is found explicitly. However, the calculations therein are complex, and for many practical situations the approach of this paper is found sufficient.

of how $v_b(x)$ is calculated for a beam on flexible supports are provided in Appendix A.

The governing equations for the horizontal (u) and vertical (v) displacements in the extended beam (elastic layer) of Fig. 2(b), assuming plane strain, are given by

$$\frac{2(1-\nu)}{1-2\nu}\frac{\partial^2 u}{\partial x^2} + \frac{\partial^2 u}{\partial y^2} + \frac{1}{1-2\nu}\frac{\partial^2 v}{\partial x \partial y} = 0 \tag{1a}$$

and

$$\frac{\partial^2 v}{\partial x^2} + \frac{2(1-\nu)}{1-2\nu}\frac{\partial^2 v}{\partial y^2} + \frac{1}{1-2\nu}\frac{\partial^2 u}{\partial x \partial y} = 0, \tag{1b}$$

which reflect horizontal and vertical linear momentum balance, respectively; see, e.g. Timoshenko and Goodier (1970, p. 241) or Sadd (2005, p. 125). The boundary conditions may be taken to be

$$\sigma_{xy} = 0, \quad \sigma_{yy} = -P_c(x) \quad \text{on the top surface, i.e. at } y = 0, \tag{2a}$$

and

$$\sigma_{xy} = 0, \quad v = v_b(x) \quad \text{on the bottom surface, i.e. at } y = h. \tag{2b}$$

We now follow Sneddon (1995, p. 402) to map the above problem into Fourier space by transforming the x coordinate. Solving for the vertical displacement in Fourier space and, then, taking the inverse Fourier transform yields the following integral equation for the vertical displacement of the top surface:

$$v(x,0) = -\frac{2}{\pi E^*}\int_0^\infty \bar{P}_c(\xi)\frac{\sinh^2 \xi h}{\xi(\xi h + \sinh \xi h \cosh \xi h)}\cos \xi x\, d\xi$$
$$+ \frac{1}{\pi}\int_0^\infty \bar{v}_b(\xi)\frac{\sinh \xi h + \xi h \cosh \xi h}{\xi h + \sinh \xi h \cosh \xi h}\cos \xi x\, d\xi, \tag{3}$$

where $E^* = E/(1-\nu^2)$,

$$\bar{P}_c(\xi) = \int_{-\infty}^\infty -P_c(t)\cos \xi t\, dt \quad \text{and} \quad \bar{v}_b(\xi) = \int_{-\infty}^\infty v_b(t)\cos \xi t\, dt. \tag{4}$$

Appendix B provides details of how (3) is obtained. For non-dimensionalizing it is more convenient to rewrite (3) as

$$v(x,0) = \frac{2}{\pi E^*}\int_0^\infty \int_{-\infty}^\infty P_c(t)\cos \xi t\, dt\frac{\sinh^2 \xi h}{\xi(\xi h + \sinh \xi h \cosh \xi h)}\cos \xi x\, d\xi$$
$$+ \frac{1}{\pi}\int_0^\infty \int_{-\infty}^\infty v_b(t)\cos \xi t\, dt\frac{\sinh \xi h + \xi h \cosh \xi h}{\xi h + \sinh \xi h \cosh \xi h}\cos \xi x\, d\xi, \tag{5}$$

where we have invoked definitions (4) of $\bar{P}_c$ and $\bar{v}_b$.

In contact problems the vertical displacement within the contact region is constrained. For example, during indentation with a rigid punch, the surface in the contact region must conform to the shape of the punch. We now approximate the profile of the cylindrical punch of radius R as a parabola in the contact region, as is appropriate if the indentation depth and the dimensions of the contact region are much smaller than the radius of curvature of the punch. We set δ to be the vertical displacement of the punch. This allows us to write the vertical displacement of the beam's top surface within the contact region as

$$v(x,0) = \delta - \frac{x^2}{2R}, \quad -a \leq x \leq a, \tag{6}$$

where the contact region lies between $-a$ and a.

During contact, the pressure on the beam's top surface depends also on the adhesive interaction between the beam and the punch. This adhesive interaction is, in turn, introduced through the presence of an adhesive zone; see inset of Fig. 2(b). Within the adhesive zone the adhesive interaction is modeled through a Dugdale–Barenblatt model (Maugis, 1992), which assumes the adhesion to

be of constant strength σ_0. Thus, we may write the force distribution on the beam's top surface as

$$P_c(x) = \begin{cases} p(x), & |x| \leq a \\ -\sigma_0, & a < |x| \leq c \\ 0, & |x| > c, \end{cases} \tag{7}$$

where c locates the outer edge of the adhesive zone; see inset in Fig. 2(b). Adhesive zones were introduced by Maugis (1992) in order to avoid the singularity in the pressure at the contact edge ($x = \pm a$) found in JKR theory. For this, it is also necessary that there be no discontinuity in the contact pressure at the contact edge, i.e.

$$\lim_{x \to \pm a^-} p(x) = -\sigma_0. \tag{8}$$

To close our mathematical description we require an additional equation to compute the extent c of the adhesive zone. This is obtained by equating the energy release rate computed from the $J-$integral (Rice, 1968) and the work of adhesion w, which leads to

$$\sigma_0 \delta_c = w, \tag{9}$$

where

$$\delta_c = (c^2/2R) - \delta + v_c \tag{10}$$

is the air-gap at which the adhesive forces vanish and $v_c = v(c,0)$; see inset in Fig. 2(b).

During non-adhesive indentation (10) is automatically satisfied as $\sigma_0 = 0 = w$. The JKR approximation is obtained in the limits $\sigma_0 \to \infty$ and $c \to a$, at which the energy balance (9) becomes

$$\frac{K_1^2}{2E^*} = w, \tag{11}$$

where

$$K_1 = -\lim_{x \to a^-}\sqrt{2\pi(a-x)}p(x) \tag{12}$$

is the *stress intensity factor* that measures the strength of the square root singularity in the stress field at the contact edge; see Maugis (1992). This is equivalent to Griffith's criterion in fracture mechanics; see e.g. Kanninen and Popelar (1985, p. 168). In this limit, we do not require the contact pressure end condition (8).

Finally, the total load acting on the punch is found by integrating the normal traction over the top surface of the beam:

$$P = \int_{-\infty}^\infty P_c(x)\, dx = \int_{-a}^a p(x)\, dx - 2\sigma_0(c-a). \tag{13}$$

3. Non-dimensionalization

We introduce the following non-dimensional parameters:

$$A = \frac{a}{l}; \quad \varphi(\tau) = \frac{aRl}{Kh^3}p(a\bar{\tau}); \quad \bar{P} = \frac{PRl}{Kh^3}; \quad k_t^f = \frac{k_t l}{EI}; \quad k_s^f = \frac{k_s l^3}{EI};$$

$$\Delta = \frac{\delta R}{l^2}; \quad L = \frac{l}{R}; \quad \lambda = 2\sigma_0\left(\frac{R}{\pi wK^2}\right)^{1/3}; \quad m = \left(\frac{\pi w}{RK}\right)^{1/3},$$

where $K = 4E^*/3$ and $I = h^3/12$ is the beam's area moment of inertia. We also define the scaled variables

$$\{\bar{x}, \bar{\tau}, \bar{c}, \bar{\gamma}\} = \frac{1}{a}\{x, t, c, h\}; \quad \{\hat{\tau}, \hat{\gamma}\} = \frac{1}{l}\{t, h\};$$

$$\{\omega, \bar{\omega}, \hat{\omega}\} = \left\{\xi h, \frac{\omega}{\bar{\gamma}}, \frac{\omega}{\hat{\gamma}}\right\};$$

$$\{\vartheta(\bar{x}, 0), \vartheta_b(\hat{\tau})\} = \frac{R}{l^2}\{v(\bar{x}, 0), v_b(l\hat{\tau})\};$$

$$\bar{I} = \frac{I}{h^3} = \frac{1}{12}; \quad \Phi(\tau) = \frac{aRl}{Kh^3}P_c(a\bar{\tau}).$$

In terms of these variables the non-dimensional vertical displacement of the top surface (5) becomes

$$\vartheta(\bar{x}, 0) = \frac{8\hat{\gamma}^3}{3\pi} \int_0^\infty \int_{-\infty}^\infty \Phi(\bar{\tau}) \cos \bar{\omega}\bar{\tau} \, d\bar{\tau} \, K_1(\bar{\omega}, \bar{x}) \, d\omega$$
$$+ \frac{1}{\pi\hat{\gamma}} \int_0^\infty \int_{-\infty}^\infty \vartheta_b(\hat{\tau}) \cos \hat{\omega}\hat{\tau} \, d\hat{\tau} \, K_2(\bar{\omega}, \bar{x}) \, d\omega, \quad (14)$$

with the kernels

$$K_1(\bar{\omega}, \bar{x}) = \frac{\sinh^2 \omega}{\omega(\omega + \sinh \omega \cosh \omega)} \cos(\bar{\omega}\bar{x})$$

and $K_2(\bar{\omega}, \bar{x}) = \dfrac{\sinh \omega + \omega \cosh \omega}{\omega + \sinh \omega \cosh \omega} \cos(\bar{\omega}\bar{x})$.

From (7), we obtain the non-dimensional pressure on the beam's top surface:

$$\Phi(\bar{\tau}) = \begin{cases} \varphi(\bar{\tau}), & |\bar{\tau}| \le 1 \\ -\lambda Am/2\hat{\gamma}^3 L, & 1 < |\bar{\tau}| \le \bar{c} \\ 0, & |\bar{\tau}| > \bar{c}. \end{cases} \quad (15)$$

Combining (14) and (15) yields

$$\vartheta(\bar{x}, 0) = -\frac{8\hat{\gamma}^3}{3\pi} \int_0^\infty \bar{\varphi}(\bar{\omega}) K_1(\bar{\omega}, \bar{x}) \, d\omega$$
$$- \frac{8\lambda Am}{3\pi L} \int_0^\infty \bar{\varphi}_0(\bar{\omega}) K_1(\bar{\omega}, \bar{x}) \, d\omega$$
$$+ \frac{1}{\pi\hat{\gamma}} \int_0^\infty \hat{\vartheta}_b(\hat{\omega}) K_2(\bar{\omega}, \bar{x}) \, d\omega, \quad (16)$$

with

$$\bar{\varphi}(\bar{\omega}) = -\int_{-1}^1 \varphi(\bar{\tau}) \cos(\bar{\omega}\bar{\tau}) \, d\bar{\tau},$$

$$\bar{\varphi}_0(\bar{\omega}) = \int_1^{\bar{c}} \cos(\bar{\omega}\bar{\tau}) \, d\bar{\tau} \quad \text{and} \quad \hat{\vartheta}_b(\hat{\omega}) = \int_{-\infty}^\infty \vartheta_b(\hat{\tau}) \cos(\hat{\omega}\hat{\tau}) \, d\hat{\tau}. \quad (17)$$

Non-dimensionalizing the displacement in the contact region (6), the contact pressure end condition (8), and the energy Eq. (9) lead to, respectively,

$$\vartheta(\bar{x}, 0) = \Delta - \frac{1}{2} \bar{x}^2 A^2 \quad \text{for} \quad -1 \le \bar{x} \le 1, \quad (18)$$

$$\varphi(\pm 1) = -\frac{\lambda Am}{2\hat{\gamma}^3 L} \quad (19)$$

and $1 = \dfrac{\pi \lambda L^2}{2m^2} \left[\dfrac{\bar{c}^2 A^2}{2} - \Delta + \vartheta_c \right]$, (20)

where $\vartheta_c = \vartheta(\bar{c}, 0)$ and Δ is the non-dimensional displacement of the punch. Combining (11) and (12), and non-dimensionalizing, we obtain

$$\lim_{\bar{x} \to 1^-} \sqrt{(1 - \bar{x})} \varphi(\bar{x}) = -\frac{m}{2\pi L} \left(\frac{l}{h}\right)^3 \sqrt{\frac{3Am}{L}}, \quad (21)$$

which replaces (19) and (20) whenever we invoke the JKR approximation.

The total non-dimensional load acting on the punch is found from (13):

$$\bar{P} = \int_{-1}^1 \varphi(\bar{\tau}) \, d\bar{\tau} - \frac{\lambda Am}{\hat{\gamma}^3 L}(\bar{c} - 1). \quad (22)$$

Finally, evaluating (16) in the contact region, i.e. for $-1 \le \bar{x} \le 1$, and employing (18) we obtain

$$\Delta - \frac{1}{2} \bar{x}^2 A^2 = -\frac{8\hat{\gamma}^3}{3\pi} \int_0^\infty \bar{\varphi}(\bar{\omega}) K_1(\bar{\omega}, \bar{x}) \, d\omega$$
$$- \frac{8\lambda Am}{3\pi L} \int_0^\infty \bar{\varphi}_0(\bar{\omega}) K_1(\bar{\omega}, \bar{x}) \, d\omega$$
$$+ \frac{1}{\pi\hat{\gamma}} \int_0^\infty \hat{\vartheta}_b(\hat{\omega}) K_2(\bar{\omega}, \bar{x}) \, d\omega. \quad (23)$$

This is a Fredholm integral equation of first kind; see Polyanin and Manzhirov (2008, p. 573). Indeed, recall that we have assumed that v_b may be found approximately from Euler-Bernoulli theory after subjecting a beam to a concentrated load P at its midspan. We now solve the above equation, along with boundary conditions (19) and (20), for the contact pressure $\varphi(\bar{x})$, displacement Δ and the location $\bar{c}$ of the adhesive zone's edge, at a given contact area A.

4. Numerical solution

The integral equation (23) does not admit an analytical solution due to the complex kernels present. Thus, we solve it numerically. To this end, we approximate the unknown pressure distribution $p(x)$ in the contact region through a series of Chebyshev polynomials. Chebyshev polynomials are chosen due to their spectral convergence; see Mason and Handscomb (2003, p. 63).

The unknown non-dimensional pressure distribution is expressed as a series of Chebyshev polynomials of the first kind, viz.

$$\varphi(\bar{\tau}) = -\frac{\lambda Am}{2\hat{\gamma}^3 L} + \frac{1}{\sqrt{1 - \bar{\tau}^2}} \sum_{n=0}^N b_{2n} T_{2n}(\bar{\tau}), \quad (24)$$

where b_{2n} are unknown constants that are to be found. Only even Chebyshev polynomials are considered as the problem is symmetric[3] about the origin. The constant term in the approximation is introduced to explicitly account for the continuity condition (19) that is imposed on the contact pressure at the edge of the contact zone. The square root singularity in the approximation is chosen as it is the weight function for Chebyshev polynomials of the first kind and also to explicitly take care of the singularity found in the general solution to the contact pressure in a contact problems; see, e.g. Gladwell (1980, p. 63, 260).

Employing (24) to evaluate the integrals $\bar{\varphi}(\bar{\omega})$ and $\bar{\varphi}_0(\bar{\omega})$ from (17), we obtain, respectively,

$$\bar{\varphi}(\bar{\omega}) = \frac{\lambda Am}{\hat{\gamma}^3 L} \frac{\sin \bar{\omega}}{\bar{\omega}} - \sum_{n=0}^N b_{2n} \alpha_{2n}(\bar{\omega}) \quad (25)$$

and $\bar{\varphi}_0(\bar{\omega}) = \dfrac{1}{\bar{\omega}}(-\sin \bar{\omega} + \sin \bar{\omega}\bar{c})$, (26)

where

$$\alpha_{2n}(\bar{\omega}) = \int_{-1}^1 \frac{1}{\sqrt{(1 - \tau^2)}} T_{2n}(\bar{\tau}) \cos \bar{\omega}\bar{\tau} \, d\bar{\tau}. \quad (27)$$

Appendix C provides details of how $\alpha_{2n}(\bar{\omega})$ are computed. Combining (22) and (24), we find the total load acting on the punch to be

$$\bar{P} = \pi b_0 - \frac{\lambda Am}{\hat{\gamma}^3 L} \bar{c}. \quad (28)$$

---

[3] Pandey et al. (2014) and Plaut and Virgin. (2017) showed that the curved nonlinear beams may also assume an asymmetric configuration even when the point load is applied at the center of the beam. Here, the initial configuration of the beam is *not* curved and the beam is *not* non-linear. Hence, the beam deforms symmetrically.

The displacement of the beam's bottom surface $\hat{\vartheta}_b(\hat{\omega})$ may, with (28), be written as

$$\frac{1}{\pi\hat{\gamma}}\hat{\vartheta}_b(\hat{\omega}) = \frac{4}{3\hat{\gamma}\bar{I}(1-\nu^2)}\left(b_0 - \frac{\lambda Am\bar{c}}{\pi\hat{\gamma}^3 L}\right)\hat{\vartheta}_p(\hat{\omega}), \qquad (29)$$

where $\bar{I}$ is the scaled area moment of inertia, and the exact form of $\hat{\vartheta}_p$ depends upon how the beam is supported at its ends; see Appendix A.

The vertical displacement in the contact region may be expressed in terms of Chebyshev polynomials as

$$\Delta - \frac{1}{2}\bar{x}^2 A^2 = \sum_{n=0}^{N} a_{2n} T_{2n}(\bar{x}) = \left(\Delta - \frac{A^2}{4}\right)T_0(\bar{x}) - \frac{A^2}{4}T_2(\bar{x}). \qquad (30)$$

Employing expansions (24)–(30) in the integral equation (23), we obtain

$$\sum_{n=0}^{N} a_{2n} T_{2n}(\bar{x}) = \frac{8\hat{\gamma}^3}{3\pi}\sum_{n=0}^{N} b_{2n}\mathcal{J}_{2n}^{(1)}(\bar{x}) - \frac{8\lambda Am}{3\pi L}\mathcal{J}^{(1)}(\bar{x})$$
$$+ \frac{4}{3\hat{\gamma}\bar{I}(1-\nu^2)}\left(b_0 - \frac{\lambda Am\bar{c}}{\pi\hat{\gamma}^3 L}\right)\mathcal{J}^{(2)}(\bar{x}), \qquad (31)$$

where

$$\mathcal{J}_{2n}^{(1)}(\bar{x}) = \int_0^\infty \alpha_{2n}(\bar{\omega})\,K_1(\bar{\omega},\bar{x})\,\mathrm{d}\omega,$$
$$\mathcal{J}^{(1)}(\bar{x}) = \int_0^\infty \frac{\sin\bar{\omega}\,\bar{c}}{\bar{\omega}}\,K_1(\bar{\omega},\bar{x})\,\mathrm{d}\omega$$

and $\mathcal{J}^{(2)}(\bar{x}) = \int_0^\infty \hat{\vartheta}_p(\hat{\omega})\,K_2(\bar{\omega},\bar{x})\,\mathrm{d}\omega.$

We evaluate the above integrals at any $\bar{x}$ through the Clenshaw–Curtis quadrature (Press et al., 1992, p. 196). We now follow Gladwell (1980, p. 267) and utilize Galerkin projections to solve (31) for the unknown coefficients b_{2n}. To this end, we multiply both sides of (31) by $T_{2m}(\bar{x})/\sqrt{1-\bar{x}^2}$, for $m = 0, \cdots, N$, and integrate from $\bar{x} = -1$ to $\bar{x} = 1$. This yields the following system of $N+1$ linear algebraic equations:

$$\sum_{n=0}^{N} a_{2n}\mathcal{J}_{nm} = \frac{8\hat{\gamma}^3}{3\pi}\sum_{n=0}^{N} b_{2n}\mathcal{J}_{nm}^{(1)} - \frac{8\lambda Am}{3\pi L}\mathcal{J}_m^{(1)}$$
$$+ \frac{4}{3\hat{\gamma}\bar{I}(1-\nu^2)}\left(b_0 - \frac{\lambda Am\bar{c}}{\pi\hat{\gamma}^3 L}\right)\mathcal{J}_m^{(2)}, \qquad (32)$$

where

$$\mathcal{J}_{nm} = \int_{-1}^1 \frac{T_{2n}(\bar{x})\,T_{2m}(\bar{x})}{\sqrt{1-\bar{x}^2}}\,\mathrm{d}\bar{x}, \quad \mathcal{J}_{nm}^{(1)} = \int_{-1}^1 \frac{\mathcal{J}_{2n}^{(1)}(\bar{x})\,T_{2m}(\bar{x})}{\sqrt{1-\bar{x}^2}}\,\mathrm{d}\bar{x},$$
$$\mathcal{J}_m^{(1)} = \int_{-1}^1 \frac{\mathcal{J}^{(1)}(\bar{x})\,T_{2m}(\bar{x})}{\sqrt{1-\bar{x}^2}}\,\mathrm{d}\bar{x} \quad \text{and}\,\mathcal{J}_m^{(2)} = \int_{-1}^1 \frac{\mathcal{J}^{(2)}(\bar{x})\,T_{2m}(\bar{x})}{\sqrt{1-\bar{x}^2}}\,\mathrm{d}\bar{x}.$$

The foregoing integrals are evaluated through a Gauss–Chebyshev quadrature (Gladwell, 1980, p. 260).

Equations for b_{2n}, Δ and $\bar{c}$ are now obtained. Employing expansion (24) in the contact pressure end condition (19) yields

$$b_0 + b_2 + \cdots + b_{2N} = 0. \qquad (33)$$

The energy balance (20) provides

$$\frac{\pi\lambda L^2}{2m^2}\left(\frac{\bar{c}^2 A^2}{2} - \Delta + \vartheta_c\right) = 1, \qquad (34)$$

where the non-dimensional displacement of the punch

$$\Delta = \frac{8\hat{\gamma}^3}{3\pi}\sum_{n=0}^{N} b_{2n}\mathcal{J}_{2n}^{(1)}(0) - \frac{8\lambda Am}{3\pi L}\mathcal{J}^{(1)}(0)$$
$$+ \frac{4}{3\hat{\gamma}\bar{I}(1-\nu^2)}\left(b_0 - \frac{\lambda Am\bar{c}}{\pi\hat{\gamma}^3 L}\right)\mathcal{J}^{(2)}(0), \qquad (35)$$

and the air gap at the end of the adhesive zone is

$$\vartheta(\bar{c}) = \frac{8\hat{\gamma}^3}{3\pi}\sum_{n=0}^{N} b_{2n}\mathcal{J}_{2n}^{(1)}(\bar{c}) - \frac{8\lambda Am}{3\pi L}\mathcal{J}^{(1)}(\bar{c})$$
$$+ \frac{4}{3\hat{\gamma}\bar{I}(1-\nu^2)}\left(b_0 - \frac{\lambda Am\bar{c}}{\pi\hat{\gamma}^3 L}\right)\mathcal{J}^{(2)}(\bar{c}). \qquad (36)$$

Finally, we have $N+1$ equations from (32) and one each from (33) and (34), for a total of $N+3$ equations. For a given contact area A, the total number of unknowns in this problem are also $N+3$: the unknown coefficients b_{2n}, with $n = 0, \cdots, N$ in the expansion (24) of the contact pressure $\varphi(\bar{x})$, the displacement Δ of the punch, and the location $\bar{c}$ of the adhesive zone's edge.

The system of Eqs. (32)–(34) are linear in b_{2n} and Δ, but *non-linear* in $\bar{c}$; cf. (34). Thus, an iterative procedure is followed beginning with an initial guess for $\bar{c}$. At any $\bar{c}$, (32) and (33) are solved for b_{2n} and Δ. These b_{2n} and Δ must satisfy (34) at the current value of $\bar{c}$. If (34) is not satisfied, then the value of $\bar{c}$ is updated through a Newton–Raphson root finding algorithm; see, e.g. Chatterjee (2002). We continue to iterate until a consistent set of b_{2n}, Δ and $\bar{c}$ is found. Care should be taken while finding the adhesive zone size $\bar{c}$, as it depends sensitively on the initial guess, and on the root finding algorithm that is employed. Once b_{2n}, Δ and $\bar{c}$ are found, the contact pressure $\varphi(\bar{x})$ and the total load $\bar{P}$ may be obtained from (24) and (28), respectively.

5. Finite element simulations

For comparison later, we will also solve the non-adhesive ('Hertzian') contact of a rigid punch with a beam through the finite element (FE) method. We employ the commercial FE package ABAQUS. While ABAQUS does provide some cohesive zone models that may be employed to simulate adhesive contact, they are not easily compared with the Dugdale–Barenblatt model that we employ. Thus, we restrict comparisons with FE results to non-adhesive contact. We also limit FE simulations to clamped and simply supported beams.

In our FE simulations, the beam is modeled as a linear elastic layer with Young's modulus $E = 2000$ MPa and Poisson's ratio $\nu = 0.3$. The beam's thickness and half-span are taken as $h = 4$ mm and $l = 40$ mm, respectively. We note that these material properties are not typical of beams employed in structural adhesives, for example by Arul and Ghatak (2008). However, these properties are selected as their magnitudes allow us to easily distinguish the effect of external inputs to the punch.

The cylindrical punch has radius $R = 225$ mm and Young's modulus $E_p = 2 \times 10^6$ MPa - a thousand times the Young's modulus of the beam. A high E_p is chosen in order to approximate a rigid punch.

In our FE analysis, plane-strain elements are considered for both the beam and the punch. The load is applied on the punch. The remaining contact parameters, i.e. contact pressure, contact area, and the displacement of the punch, are obtained after post-processing the computation's output. These parameters are now compared with the semi-analytical results of Section 4.

6. Results: non-adhesive ('Hertzian') contact

We first investigate the adhesionless contact of a rigid punch with elastic beams. We will consider beams that are clamped, sim-

(a)

(b)
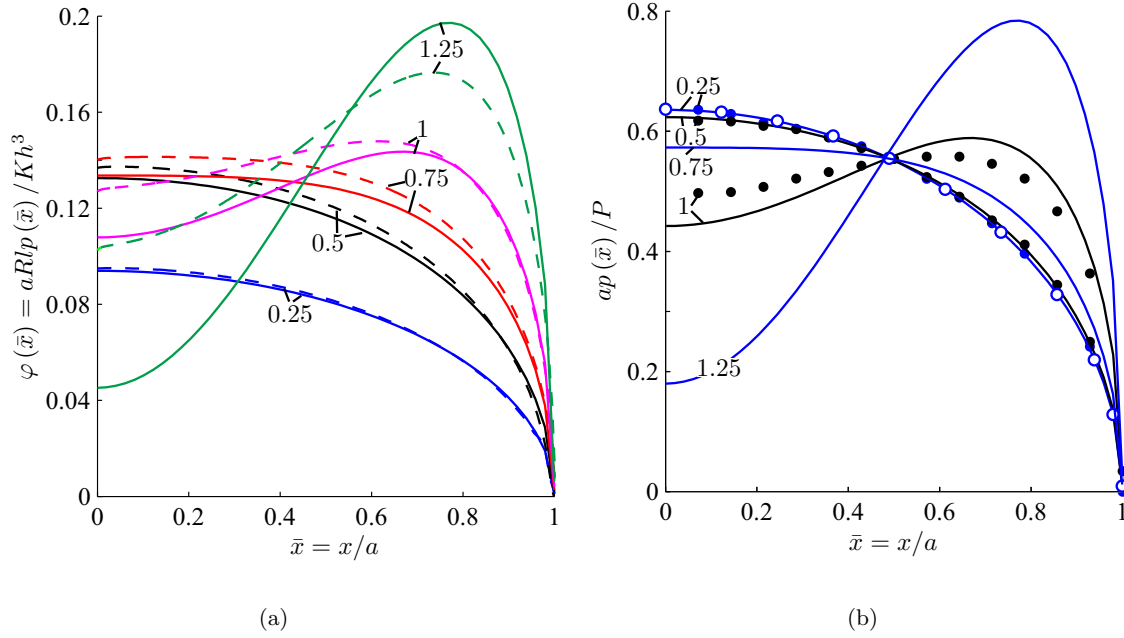
Fig. 3. Non-adhesive contact of a clamped beam. Non-dimensional contact pressures (a) $\varphi(\bar{x})$ and (b) $ap(\bar{x})/P$ are shown. The beam's slenderness ratio $l/h = 10$. Several contact areas a are investigated by varying a/h, which are noted next to their associated curves. Solid lines are results obtained from the semi-analytical procedure of Section 4. Dashed lines in (a) correspond to FE simulations of Section 5. Open-circles in (b) represent the solution for an elastic half-space. Results of Keer and Miller (1983), when available, are shown in (b) by filled circles.

ply supported, or rest on flexible supports. Some results will be compared with FE simulations of Section 5.

Equations for the indentation of a non-adhesive beam are obtained by setting $\lambda = 0$ in (32):

$$\sum_{n=0}^{N} a_{2n} \mathcal{J}_{nm} = \frac{8\hat{\gamma}^3}{3\pi} \sum_{n=0}^{N} b_{2n} \mathcal{J}_{nm}^{(1)} + \frac{4b_0}{3\hat{\gamma}\hat{I}(1-\nu^2)} \mathcal{J}_m^{(2)} \quad \text{for } m = 0, \cdots, N.$$

(37)

The contact pressure vanishes at the edge $\bar{x} = \pm 1$ of the contact zone, so that (33) holds. The energy condition (34) is now redundant. The $N + 2$ equations that comprise (33) and (37) are to be solved for the $N + 2$ unknowns b_{2n} ($n = 0, \cdots, N$) and Δ for a given choice of A. The contact pressure distribution and the total load are then found from (24) and (28), respectively, after setting $\lambda = 0$.

Computations are carried out with $N = 5$, i.e. the expansion (24) is truncated at the Chebyshev polynomial T_{10}. In all cases we report the response of contact area and punch's displacement against the total load acting on punch in the main text. In Appendix D, we report the behavior of contact area with the displacement of punch.

6.1. Clamped beam

A clamped beam is obtained in the limit of k_s^f, $k_t^f \to \infty$. Thus, $\hat{\vartheta}_p(\hat{\omega})$ is given by (A.15), which then enters into the computation of $\mathcal{J}_m^{(2)}$ in (37). The unknown contact pressure distribution $\varphi(\bar{x})$ is obtained by solving (37) and (33).

We compare the results of our semi-analytical procedure of Section 4 with FE simulations in Fig. 3(a) and with the results of Keer and Miller (1983) in Fig. 3(b). We observe from Fig. 3 that, when the ratio a/h of the contact area to the beam's thickness is low, the maximum contact pressure is obtained at the center of the contact region. We also find from Fig. 3(b) that at low a/h ratios the pressure profiles are similar to the pressure distribution obtained for indentation into an elastic half-space. Increasing the

a/h ratio – which, for a given beam (fixed h and l) corresponds to increasing the load, as the contact area increases – causes the pressure at the center of the contact region to decrease, but increase near its ends; thus, the pressure profiles acquire a double-humped character. Our semi-analytical results are in good agreement with those of FE simulations, and the theoretical results of Keer and Miller (1983) for $a/h \lesssim 1$; see Fig. 3(a) and (b), respectively. For $a/h > 1$, our assumption that the displacement of the beam's bottom surface may be approximated through Euler-Bernoulli beam theory breaks down. This causes the semi-analytical results to deviate from those of FE computations in Fig. 3(a).

We have followed Keer and Miller (1983) in plotting $ap(\bar{x})/P$ along the vertical axis in Fig. 3(b). A match employing this scale may not guarantee a correspondence of the actual pressure profiles $\varphi(\bar{x})$ or $p(\bar{x})$. This is because the total load P in the denominator of $ap(\bar{x})/P$ is calculated by integrating $\varphi(\bar{x})$ in the numerator. Thus, even if a constant factor is missed in $p(\bar{x})$, the ratio $ap(\bar{x})/P$ will remain unaffected. Given this, the comparison of pressure profiles shown in Fig. 3(a) is more illuminating. Finally, the pressure profiles in Fig. 3(b) do not vary much with the slenderness ration l/h. These plots may therefore be utilized to estimate pressures at other l/h as well.

Next, the variation of the contact area A and the displacement Δ of the punch with the total load $\bar{P}$ are shown in Fig. 4. Results of both clamped and simply supported beams (discussed in the next section) are shown. From Fig. 4(a) we find that to obtain the same contact area A, a clamped beam requires higher load compared to the simply supported beam. This outcome is expected, as the rotational play at the ends of the clamped beam is lower than that of a simply supported beam. Thus, the contribution to vertical displacement Δ from the beam's bending is lowered in the case of a clamped beam. Similarly, a clamped beam wraps less about the punch, thereby lowering the contact area at given load. The clamped beam's greater bending stiffness compared to that of a simply supported beam is clearly demonstrated by Fig. 4(b) that plots the deflection of the beam's center point – which equals the punch's displacement Δ – against the total load $\bar{P}$. The lin-

(a)   (b)
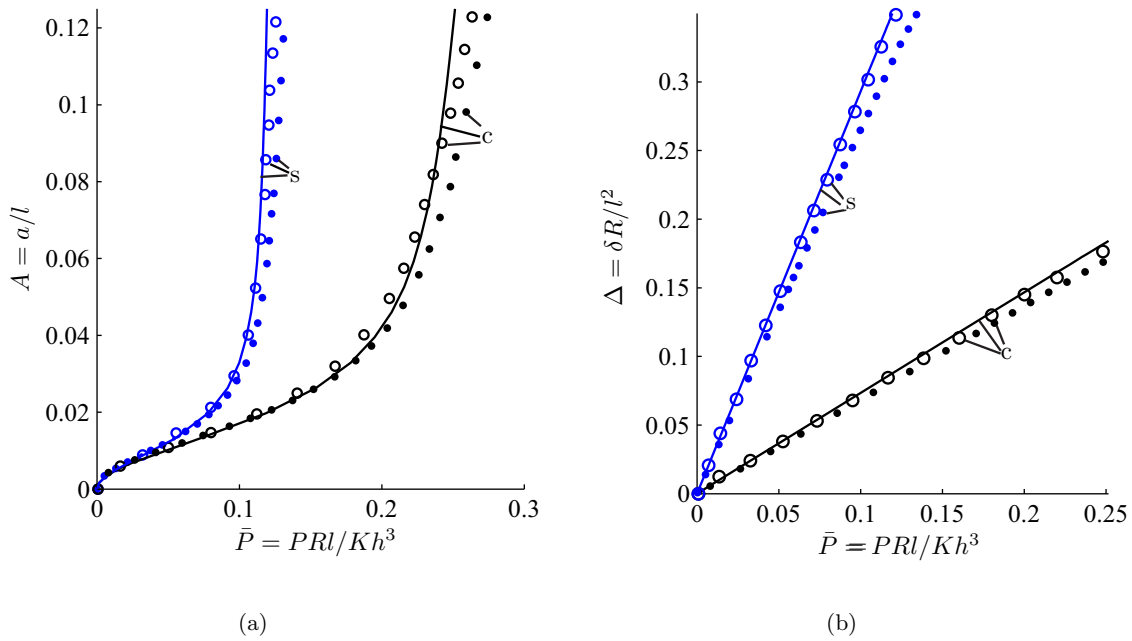
Fig. 4. Non-adhesive contact of clamped ('c') and simply supported ('s') beams. Variation of (a) the contact area A and (b) the punch's displacement Δ are plotted as a function of the total load $\bar{P}$ acting on the punch. The beam's slenderness ratio l/h=10. Solid lines are results obtained from the semi-analytical procedure of Section 4. Filled circles correspond to FE simulations of Section 5. Predictions of Sankar and Sun (1983) are shown by open circles, when available.

(a)   (b)
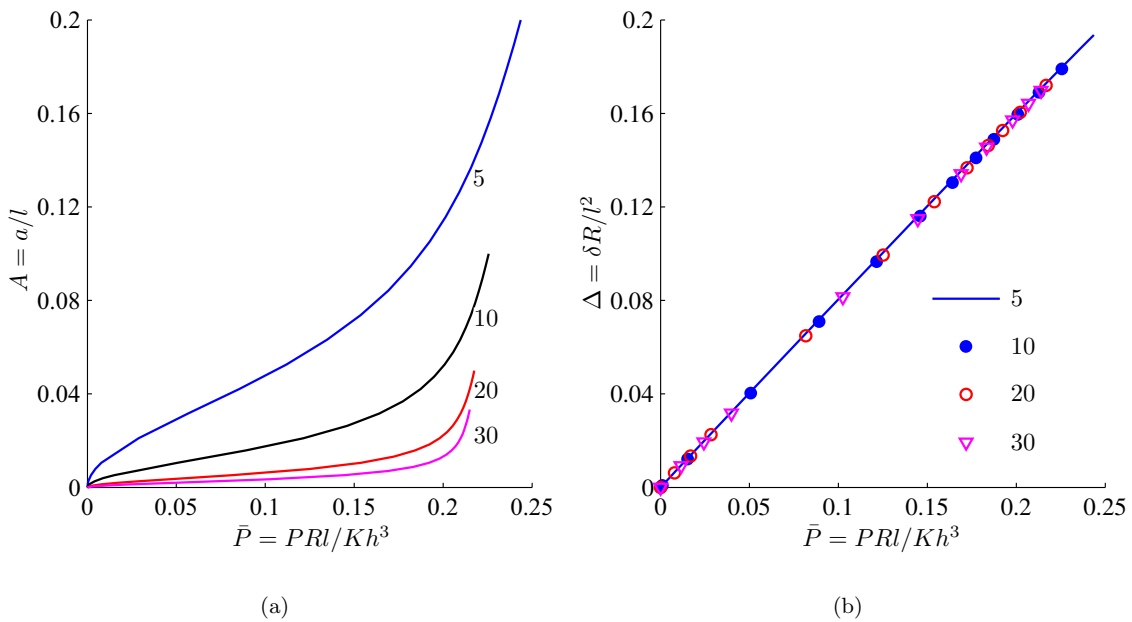
Fig. 5. Non-adhesive contact of clamped beams. Variation of (a) the contact area A and (b) the punch's displacement Δ with total load $\bar{P}$ are shown. Different slenderness ratios l/h are considered and these are noted either next to their associated curves or in the legend.

ear response of Δ with $\bar{P}$ is not unexpected as the displacement of the beam's bottom surface is obtained from beam theory. From Fig. 4 (and also Fig. D.19) it is evident that end supports have significant bearing on the beam's indentation. Finally, in Fig. 4, we again find a good match both with FE simulations and with the results of Sankar and Sun (1983).

As mentioned in Section 5, the material parameters employed in FE simulations may not be relevant for typical applications. Thus, in Fig. 5 we report results with parameters more commonly encountered. Following Dalmeya et al. (2012), the Young's modulus and Poisson's ratio of the beam are taken corresponding to

those observed in soft materials: $E = 0.083$ MPa and $\nu = 0.4$, respectively. The beam's geometry remains the same as before.

The contact area A is plotted against the total load acting on the punch $\bar{P}$ in Fig. 5(a) for clamped beams of different slenderness ratios l/h. A more slender beam is less resistant to bending. Thus, beams with higher l/h should require less load P compared to lower l/h to achieve the same contact area a. But, the curves in Fig. 5(a), do not conform to this expectation, as the non-dimensional terms A and $\bar{P}$ are expressed using the beam's geometric parameters, i.e. l and h. This phenomenon is demonstrated clearly in Fig. D.20, where we plot the variation of contact area

(a)

(b)
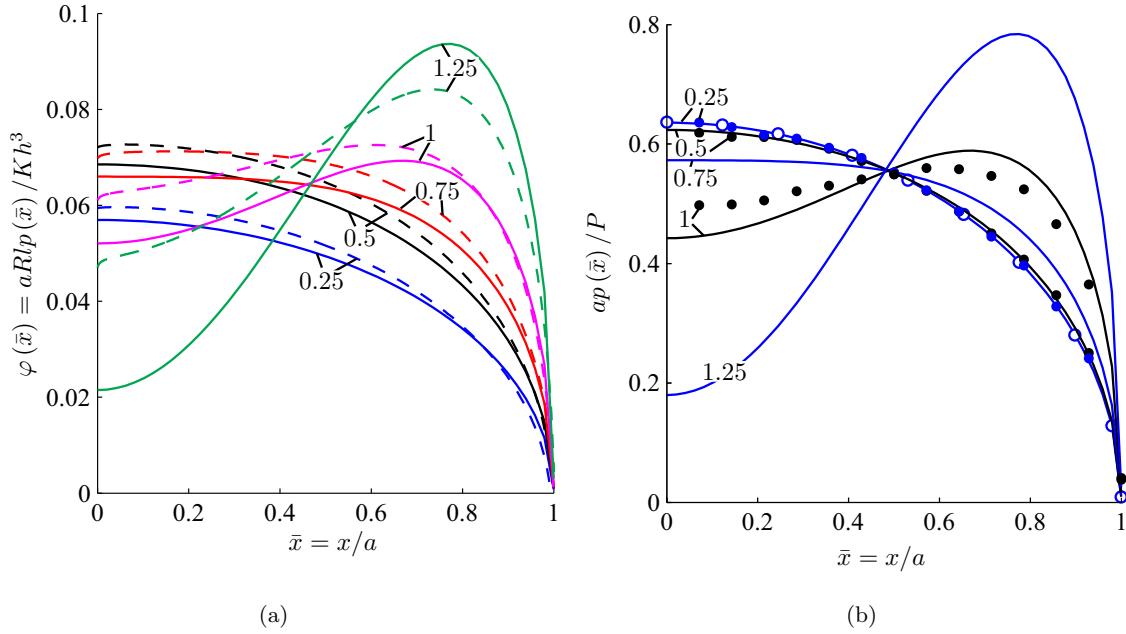
Fig. 6. Non-adhesive contact of a simply supported beam. Non-dimensional contact pressure (a) $\varphi(\bar{x})$ and (b) $ap(\bar{x})/P$ are shown. Several contact areas are investigated by varying a/h as noted next to the associated curves, while keeping $l/h = 10$. Solid lines are results obtained from the semi-analytical procedure of Section 4. Dashed lines in (a) correspond to FE simulations of Section 5. Open circles in (b) represent the solution for an elastic half-space. Results of Keer and Miller (1983), when available, are shown in (b) by filled circles.

(a)

(b)
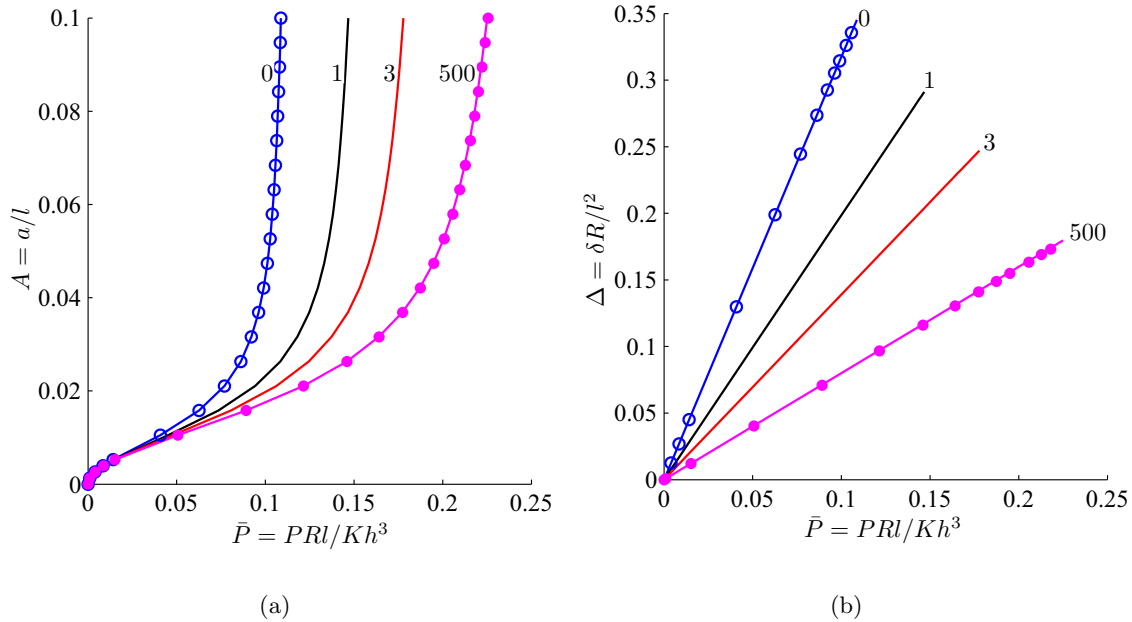
Fig. 7. Non adhesive contact of beams on flexible supports. The variation of (a) contact area A and (b) punch's displacement Δ are plotted as a function of the total load $\bar{P}$ acting on the punch. The beam's slenderness ratio $l/h = 10$. The vertical translational spring's stiffness $k_s^f = \infty$. Various torsional springs are considered and their stiffnesses k_t^f are indicated next to their associated curves. Open and filled circles represent results for simply supported and a clamped beams, respectively.

and punch displacement with the variation in total load employing new non-dimensional parameters (cf. (40)) that are free from both l and h.

Finally, in Fig. 5(b) we plot variation of the displacement Δ of the punch with the total load $\bar{P}$ for different l/h ratios. We observe that, our choice of non-dimensionalization (cf. Section 3) for the punch's displacement and the total load allows the curves in Fig. 5(b) to collapse onto a single line. This is not seen for other scalings, cf. Sections 7 and 8, where we report results for adhesive contact. We again expect the punch's displacement Δ to be high

for more slender beams. The scaled variables in Fig. 5(b) are unable to reveal this phenomenon correctly and we refer the reader to Fig. D.20(b) where this is observed clearly.

6.2. Effect of end conditions

We obtain results for a simply supported beam in the limit $k_s^f \to \infty$ and $k_t^f \to 0$. The vertical displacement of the bottom surface is given by (A.16). The contact pressure $\varphi(\bar{x})$ is then found by solving (37) and (33), and invoking (24). The behavior of a simply

(a)

(b)
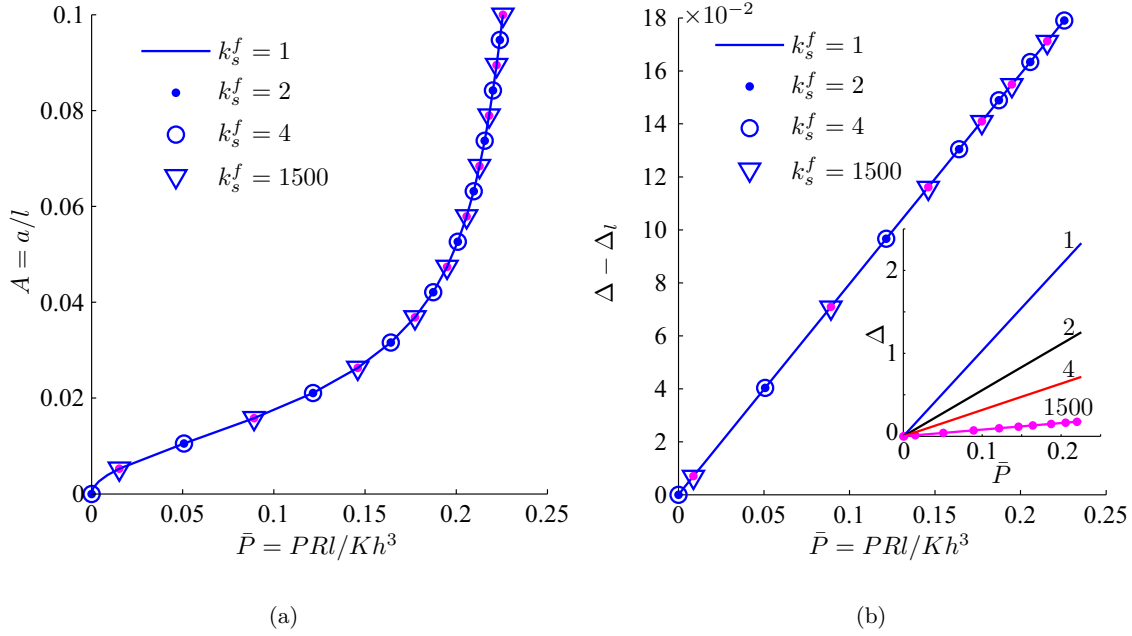
Fig. 8. Non-adhesive contact of beams on flexible supports. The variation of (a) contact area A and (b) the adjusted punch's displacement $\Delta - \Delta_l$ are plotted as a function of the total load $\bar{P}$ acting on the punch. The inset in (b) shows the variation of the punch's displacement Δ with the total load $\bar{P}$. The beam's slenderness ratio $l/h = 10$. The torsional spring stiffness $k_t^f = \infty$. Various vertical translational springs are considered and their stiffnesses k_s^f are indicated either in the legend or next to their associated curves. Filled circles in the inset in (b) represent results for a clamped beam.

(a)

(b)
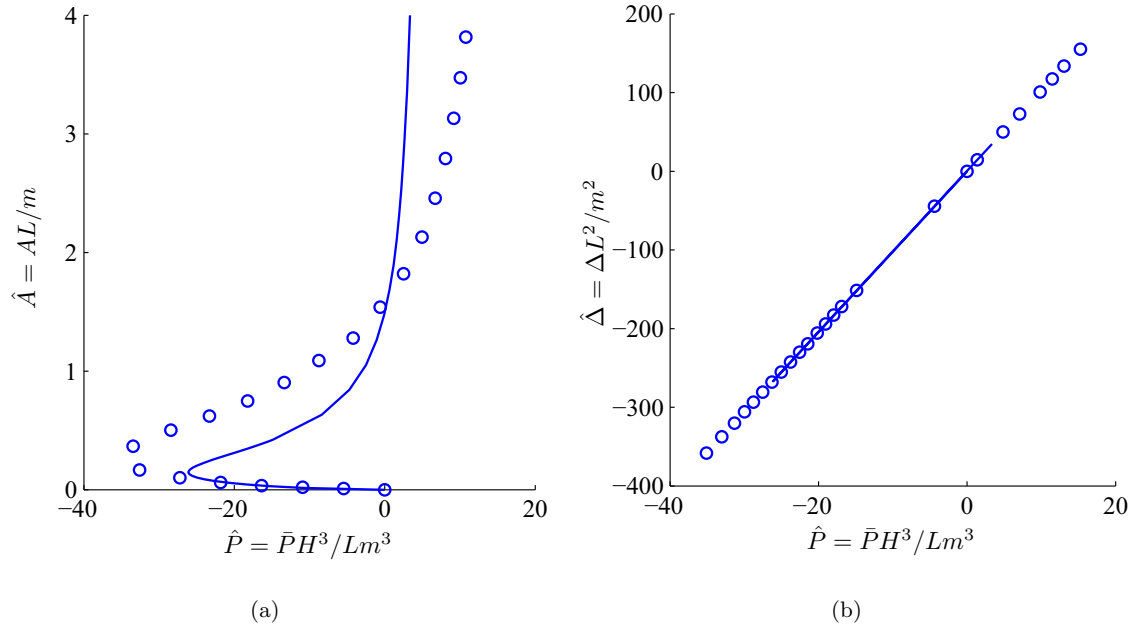
Fig. 9. Adhesive contact of clamped beams with the JKR approximation. Variation of (a) the contact area $\hat{A}$ and (b) the punch's displacement $\hat{\Delta}$ with the total load $\hat{P}$. The beam's slenderness ratio $l/h = 10$. Solid line correspond to $l = 40$ mm and $h = 4$ mm, while the open circles are for a beam with $l = 80$ mm and $h = 8$ mm.

supported beam is qualitatively similar to that of a clamped beam, but differs quantitatively.

Fig. 6 repeats Fig. 3 for simply supported beams and compare our semi-analytical results with those of FE simulations, and Keer and Miller (1983). As before, we find good agreement between all three approaches for $a/h \lesssim 1$.

Contrasting Figs. 3(a) and 6(a) we find that, at the same a/h, pressures found in a simply supported beam are lower compared to those in a clamped beam. Thus, the total load $\bar{P}$ required to achieve the same contact area, for clamped and simply supported beams of the same thickness, is very different. This reinforces the

importance of correctly modeling end supports in beam indentation. Interestingly, because of the manner in which the contact pressure is scaled, Figs. 3(b) and 6(b) are nearly the same.

Finally, we report results on the non-adhesive contact of beams resting on flexible supports with parameters utilized to generate Fig. 5. Again, for beams with slenderness ratio $l/h = 10$, the contact area A and the punch's displacement Δ are plotted against the total load $\bar{P}$ acting on the punch in Figs. 7 and 8. Fig. 7 shows results for several torsional spring stiffnesses k_t^f after setting the vertical translational spring's stiffness k_s^f to infinity. Such a beam may be thought of as a simply supported beam with some resistance to
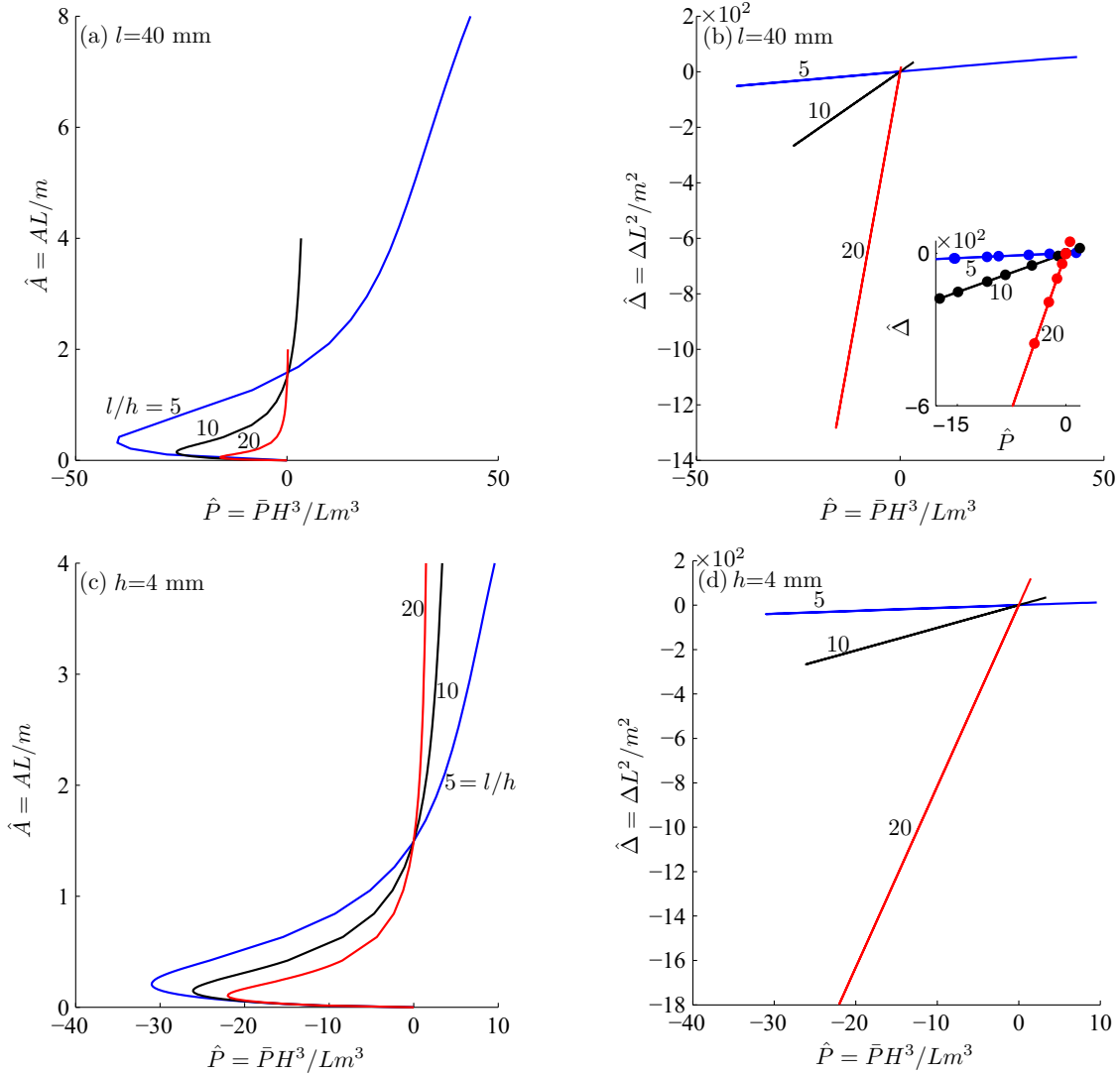
Fig. 10. Adhesive contact of clamped beams with the JKR approximation. Left column reports the variation of contact area $\hat{A}$ with total load $\hat{P}$, while the right column plots the change of punch's displacement $\hat{\Delta}$ with $\hat{P}$. Results in the top row are obtained by setting $l = 40$ mm and varying h as shown, while those in the bottom row have $h = 4$ mm but different l, as indicated. Inset in (b) is included to allow comparison with (d); filled circles in the inset represent results from (d) at the corresponding l/h.

rotation at the ends, or a beam whose clamped ends allow some rotational play. Results lie between those obtained for clamped and simply supported beams. Expectedly, increasing k_t^f shifts the results towards those of a clamped beam, and decreasing it yields results close to those of a simply supported beam. This is seen clearly in Fig. 7.

Fig. 8 repeats Fig. 7, but this time keeping k_t^f as infinity and varying k_s^f. We find that increasing k_s^f does *not* affect the variation of A with $\bar{P}$, but the dependence of Δ on P changes; see the inset in Fig. 8(b). The latter change is, however, due to the vertical displacement Δ_l of the beam's spring supports. The presence of Δ_l shifts the datum downwards, so that indentation now initiates from $y = \Delta_l$, rather than from $y = 0$. Once we correct for Δ_l we find that displacement plots in the inset of Fig. 8(b) are also unaffected by variation in k_s^f.

7. Results: adhesive contact - JKR approximation

We now consider adhesive contact of beams after invoking the JKR approximation, previously discussed in Sections 2 and 3. Thus, we need to solve the integral equation (23) along with energy bal-

ance (21), in the limit of the strength of the adhesion completely dominating elastic stiffness, i.e. $\lambda \rightarrow \infty$, while the adhesive zone becomes infinitesimally small, so that $\bar{c} \rightarrow 1$. Employing expansion (24) for the contact pressure, (23) and (21) become, respectively,

$$\sum_{n=0}^{N} a_{2n} \mathcal{J}_{nm} = \frac{8\hat{\gamma}^3}{3\pi} \sum_{n=0}^{N} b_{2n} \mathcal{J}_{nm}^{(1)} + \frac{4b_0}{3\hat{\gamma}\bar{I}(1-\nu^2)} \mathcal{J}_m^{(2)} \quad \text{for } m = 0, \cdots, N \tag{38}$$
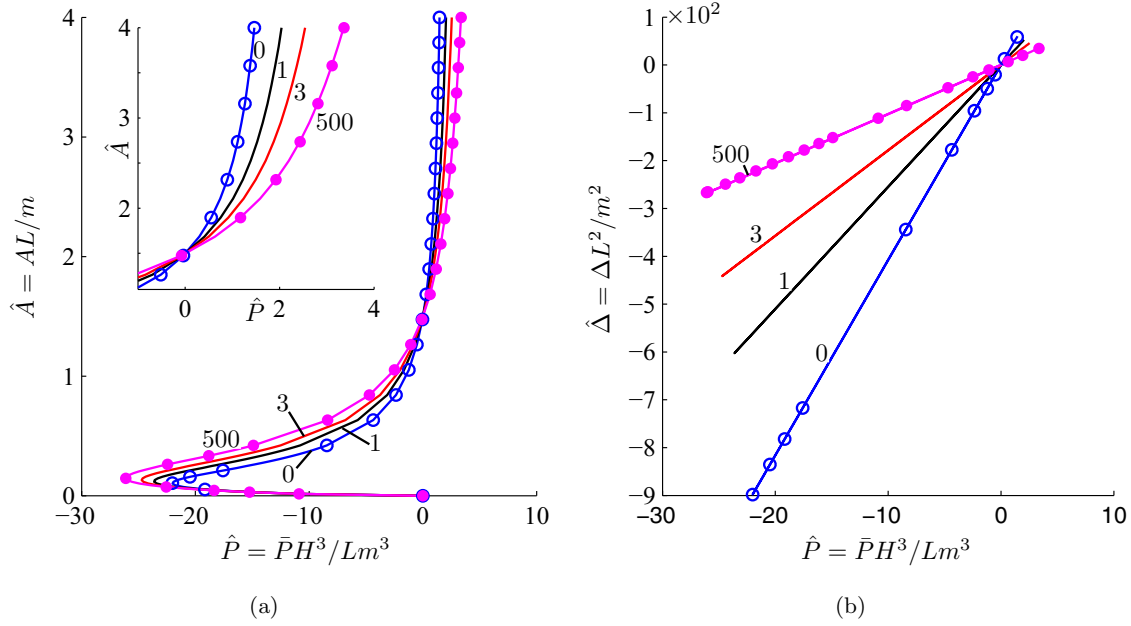
and

$$b_0 + b_2 + \cdots + b_{2N} = -\frac{m}{2\pi L}\left(\frac{l}{h}\right)^3 \sqrt{\frac{6Am}{L}}. \tag{39}$$

From hereon, we follow Maugis (1992) and employ the non-dimensional parameters

$$\hat{A} = \frac{AL}{m} = a\left(\frac{K}{\pi w R^2}\right)^{1/3},$$

$$\hat{P} = \frac{\bar{P}H^3}{Lm^3} = \frac{P}{\pi w} \quad \text{and} \quad \hat{\Delta} = \frac{\Delta L^2}{m^2} = \delta\left(\frac{K^2}{\pi^2 w^2 R}\right)^{1/3}, \tag{40}$$

Fig. 11. Adhesive contact of beam on flexible supports with the JKR approximation. Variation of (a) the contact area $\hat{A}$ and (b) the punch's displacement $\hat{\Delta}$ are plotted as a function of the total load $\hat{P}$ acting on the punch. The beam's thickness $h = 4$ mm and $l = 40$ mm. The vertical translational spring's stiffness $k_s^f = \infty$. Various torsional springs are considered and their stiffnesses k_t^f are indicated next to their associated curves. The inset in (a) correspond to behavior at high $\hat{A}$. Open and filled circles represent results for adhesive beams that are, respectively, simply supported and clamped.
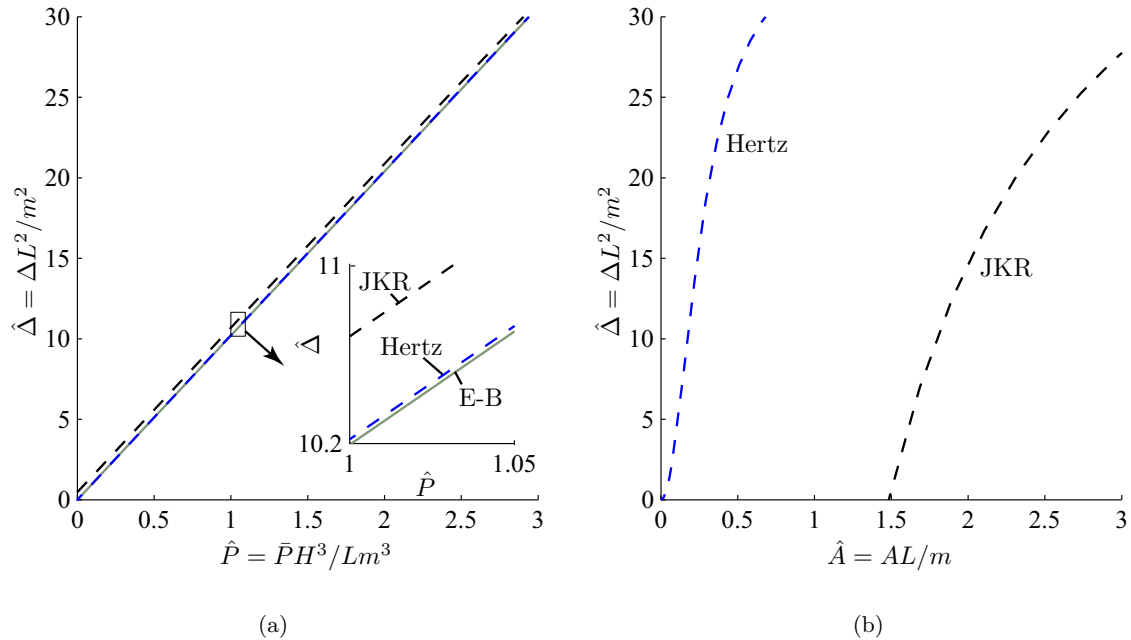

Fig. 12. Comparison of non-adhesive contact with an adhesive contact employing JKR approximation for clamped beams. Variation of the punch's displacement $\hat{\Delta}$ with (a) the load $\hat{P}$ and (b) the contact area $\hat{A}$ are reported. We set $h = 4$ mm and $l = 40$ mm. Dashed lines are for adhesive and non-adhesive (blue color online) beams following, respectively, Sections 6 and 7, while solid line represents results from Euler–Bernoulli (E-B) beam theory. Note that the contact area in E-B theory is zero. (For interpretation of the references to color in this figure legend, the reader is referred to the web version of this article.)

where $H = h/R$, instead of, respectively, A, $\bar{P}$, and Δ, to report our results. This is done in order to facilitate contact with other work on adhesion. We set the adhesion energy $w = 0.02 \times 10^{-3}$ J/mm². As in Section 6, behavior of contact area with the punch's displacement is in Appendix D.

Fig. 9 plots the variation of the contact area $\hat{A}$ and punch's displacement $\hat{\Delta}$ with the total load $\hat{P}$ acting on the punch for clamped beams. While the slenderness ratio $l/h = 10$, two different combinations of l and h are considered. From Fig. 9(a) we observe that the variation of $\hat{A}$ with $\hat{P}$ is sensitive to the choice of l

and h, notwithstanding the fact that l/h is kept constant; see also Fig. D.22(a). This is in contrast to the case of non-adhesive contact of Section 6, where results depended only on l/h. This behavior is expected for adhesive beams as the right hand side of (39) depends on $L = l/R$. However, from Fig. 9(b) we observe that the variation of $\hat{\Delta}$ with $\hat{P}$ is *not* sensitive to the choice of l and h, but only to l/h. These aspects are further highlighted in Fig. 10, which plots $\hat{A}$ and $\hat{\Delta}$ against $\hat{P}$ for clamped beams for different choices of l and h.
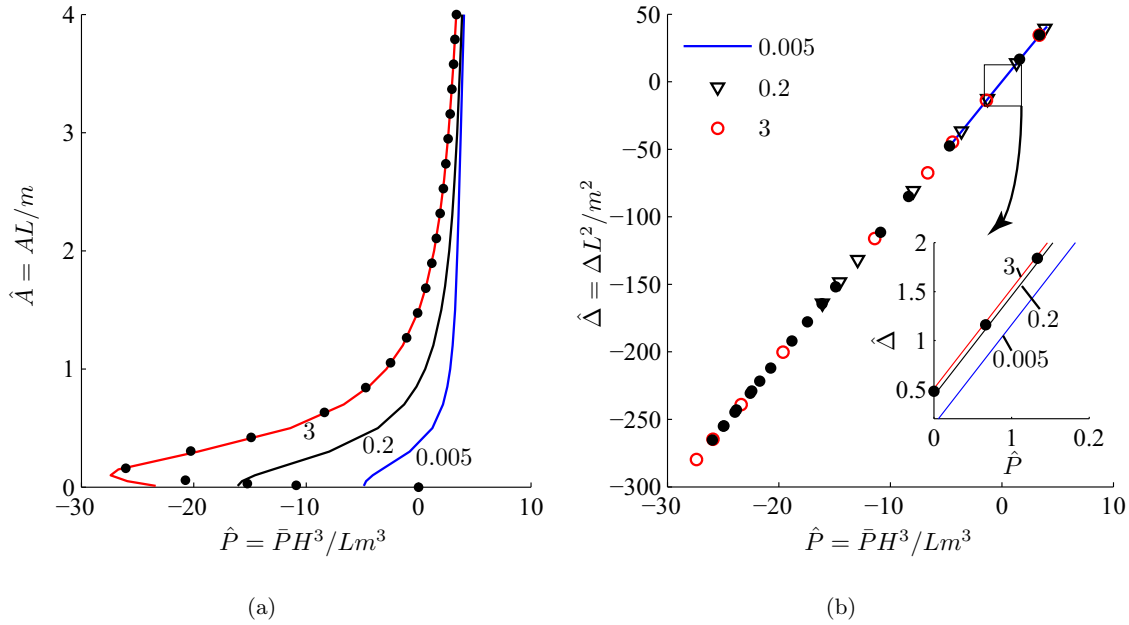
Fig. 13. Adhesive contact of clamped beams with an adhesive zone model. Variation of (a) the contact area $\hat{A}$ and (b) the punch's displacement $\hat{\Delta}$ with the total load $\hat{P}$. Different adhesive strengths λ are considered and these are indicated either next to their associated curves or in legend. The beam's thickness $h = 4$ mm and $l = 40$ mm. Filled circles represent the JKR solution for the corresponding beam; cf. Section 7.

In Figs. 9 and 10, negative values of $\hat{P}$ and $\hat{\Delta}$ reflect tensile loads and upward displacement of the punch, respectively. We recall that $\hat{\Delta}$ equals the deflection of the center point on the beam's top surface, so that $\hat{\Delta} < 0$ indicates that the beam bends upwards. Negative values of $\hat{P}$ and $\hat{\Delta}$ are due to the attractive adhesive forces. Due to adhesion, the beam bends upwards and jumps into contact. Equivalently, adhesive forces also act on the punch to pull it down, so that we require a tensile force to hold the punch in its place. This tensile force $\hat{P}$ is small for slender beams as they bend easily. For the same reason, this tensile force is smaller for a simply supported beam compared to a clamped beam of the same thickness; cf. Fig. 11. Once contact is established, the tensile force is slowly released and replaced by a compressive (downwards) force in order to increase downward indentation. Again, for compressive loads, thin beams bend more easily to wrap around the punch. Thus, slender beams show greater contact area and displacement at the same compressive load $\hat{P}$. This explains the intersection of the curves in Fig. 10. Therefore, with increasing slenderness ratio, the $\hat{A}$–$\hat{P}$ and $\hat{\Delta}$–$\hat{P}$ curves in Fig. 10 move towards (inwards) the zero-load ($\hat{P} = 0$) vertical line.

Next, for adhesive beams on flexible supports we plot the contact area $\hat{A}$ and displacement $\hat{\Delta}$ against the load $\hat{P}$ for various k_t^f in Fig. 11. Convergence to the results obtained for clamped and simply supported beams may be observed in Fig. 11 by varying k_t^f. From our discussion in Section 6.2, we know that the variation of k_s^f does not affect how the contact area $\hat{A}$ varies with the load $\hat{P}$. At the same time, change in displacement $\hat{\Delta}$ with $\hat{P}$ or $\hat{A}$ is affected by variation in k_s^f only through the vertical displacement of the translational springs supporting the beam at its ends. By removing this global displacement $\hat{\Delta}_l$ from $\hat{\Delta}$ – as in Section 6.2 – the response of $\hat{\Delta} - \hat{\Delta}_l$ to $\hat{P}$ and $\hat{A}$ to $\hat{\Delta} - \hat{\Delta}_l$ are found to be invariant to k_s^f.

Finally, in Fig. 12(a), we plot the punch's displacement $\hat{\Delta}$ in a clamped beam as a function of load $\hat{P}$ acting on the punch for three different cases: an Euler–Bernoulli beam acted upon by a point load at its midspan; an adhesionless beam modeled as in Section 6; an adhesive beam modeled using JKR approximation as above. We see that $\hat{\Delta} - \hat{P}$ curves for all cases are nearly lin-

ear with similar slopes. Adhesion increases the displacement for a given load, thereby shifting the $\hat{\Delta} - \hat{P}$ curves upward. Thus, the effective spring stiffness of indented beams closely matches the effective spring stiffness of an Euler–Bernoulli beams, irrespective of adhesion. This, to some extent, is a reflection of the current approximate model that we employ, wherein the displacement of the beam's bottom surface is approximated through Euler–Bernoulli beam theory. A more sophisticated analysis reveals that the effective spring stiffness of indented beams is non-linear and different from Euler-Bernoulli beams (Punati, 2017). It is important to note that, although the $\hat{\Delta} - \hat{P}$ curves do not differ significantly, the corresponding contact areas are very different, as is shown in Fig. 12(b). This suggests that in experiments one must also measure contact areas in order to better estimate the effect of adhesion.

8. Results: adhesive contact with an adhesive zone model

We finally consider contact with an adhesive beam within the framework of adhesive zone models. As already mentioned, we will assume that an adhesive zone of length $d = c - a$ extends outside the contact zone; cf. Fig. 2(b). Within the adhesive zone the interaction is modeled through the Dugdale–Barenblatt model of (7). To obtain the contact pressure $\varphi(\bar{x})$, the displacement Δ and the location c of the adhesive zone's edge, we have to solve (32)–(34). As in Sections 6 and 7, behavior of contact area against the punch's displacement is in Appendix D.

For the clamped beam we plot in Fig. 13 the contact area $\hat{A}$ and displacement $\hat{\Delta}$ against the total load $\hat{P}$ for various adhesive strengths λ. With increase in λ, the solutions approach the JKR solution, and we see a close match at $\lambda = 3$. On the other hand, as $\lambda \to 0$, i.e. as adhesion reduces, solutions approach those obtained for non-adhesive contact in Section 6. From Fig. 13(b) we observe that λ has limited effect on the $\hat{\Delta}$–$\hat{P}$ plots.

From previous discussions, it is expected that results for beams with flexible supports will lie between those obtained for clamped and simply supported beams. Hence, we do not explore this parameter space in great detail. We only consider the variation of $\hat{A}$ and $\hat{\Delta}$ with $\hat{P}$ for several values of torsional stiffness k_t^f for
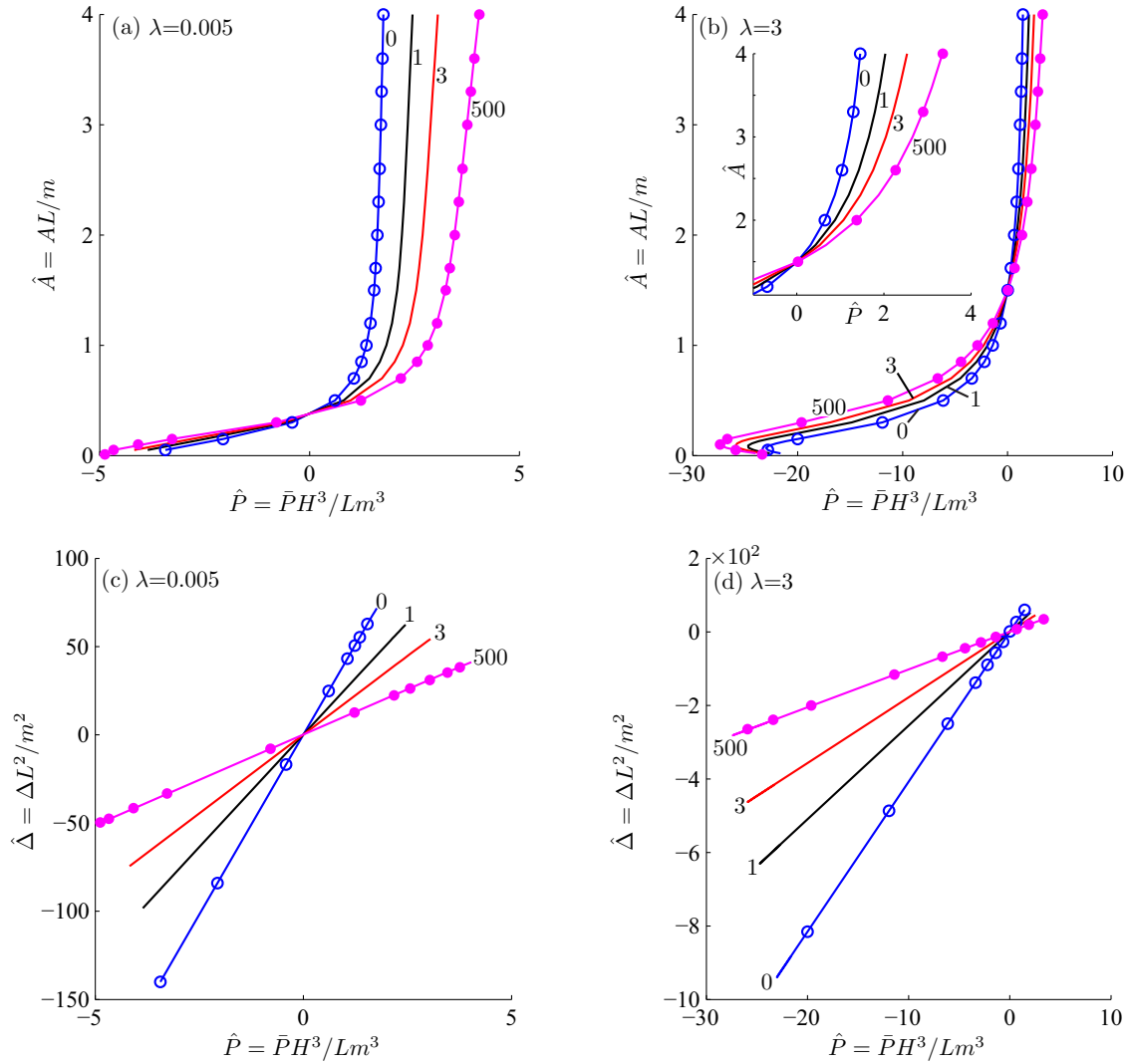
Fig. 14. Adhesive contact of beams on flexible supports with an adhesive zone model. Top row reports the variation of contact area $\hat{A}$ with total load $\hat{P}$, while the bottom row plots the change of the punch's displacement $\hat{\Delta}$ with $\hat{P}$. Different torsional spring stiffnesses k_t^f are considered, and they are noted next to their associated curves. Two different adhesive strengths λ are considered, as indicated. The beam's thickness $h = 4$ mm and half-span $l = 40$ mm. The inset in (b) depict behavior at high $\hat{A}$. Open and filled circles represent results for a simply supported and a clamped beam, respectively, at the corresponding λ.

a beam with $h = 4$ mm and $l = 40$ mm. Two different adhesive strengths λ are investigated. The results are shown in Fig. 14. The vertical translational spring's stiffness k_s^f is set to infinity. When $k_t^f = 0$, the solutions match with those of a simply supported beam with the corresponding λ. With increase in k_t^f, the solution curves move towards those obtained for a clamped beam and will coincide when k_t^f becomes infinity. It is seen in Fig. 14 that curves for different k_t^f intersect with each other due to rotation permitted at the supports by the torsional springs – greater the rotation allowed, higher the displacements, and lower the loads for the same contact area. This intersection point moves up with increasing λ, as strong adhesive forces are able to bend the beam upwards more easily.

Finally, in Fig. 15 we plot the variation of the non-dimensional adhesive zone size $\bar{d} = \bar{c} - 1$ with the contact area $\hat{A}$ for different adhesive strengths λ and various k_t^f. We observe that the adhesive zone size is large for smaller λ, and decreases with increasing λ, finally vanishing as $\lambda \to \infty$. Moreover, we find that the adhesive zone's size does not vary much with the spring stiffness k_t^f. Similarly the slenderness ratio l/h and the spring stiffness k_s^f do not affect $\bar{d}$ in any significant manner.

9. Experiments and applications

In this final section, we compare our predictions with preliminary experimental results on a clamped beam, as well as apply our methods to model structural adhesives of the type shown in Fig. 1(a).
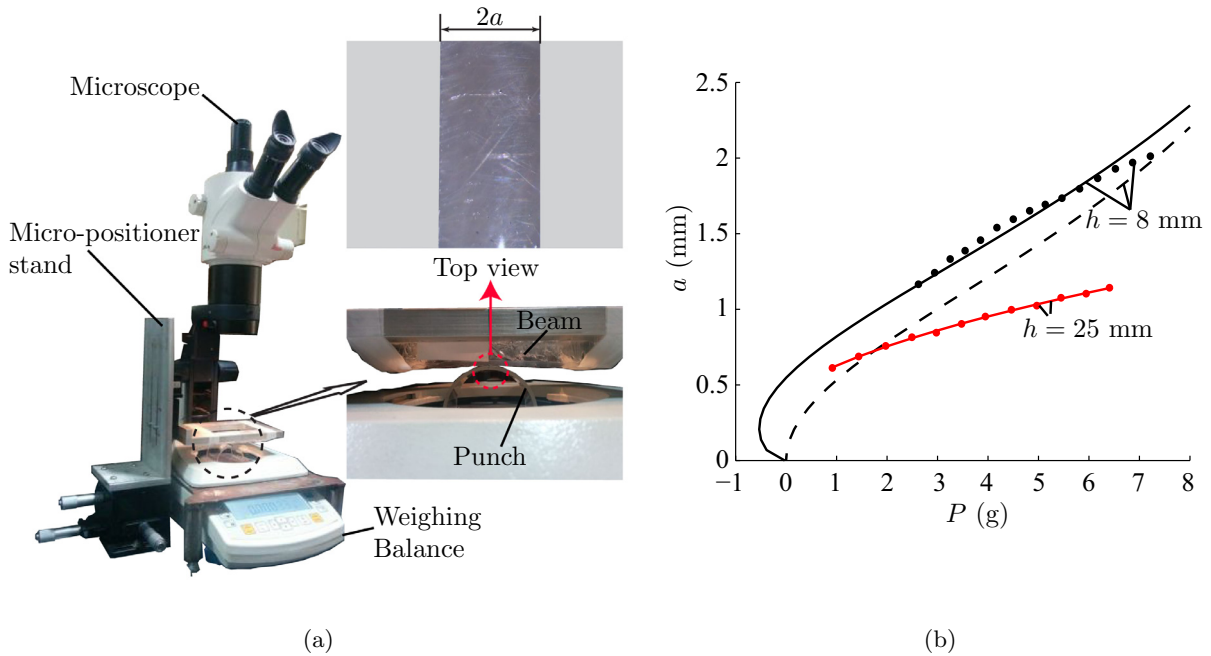
9.1. Experiments

Poly-dimethyl-siloxane (PDMS) is used to prepare the beam samples. The experimental set-up used is shown in Fig. 16(a). We followed (Chaudhury et al., 1996) to find the Young's modulus E and the work of adhesion w for our PDMS by indenting a thick ($h = 25$ mm) sample and fitting the experimental results with the JKR theory for an elastic half-space. Fig. 16(b) plots the experimental data and fitted JKR theory. We estimate E to be in the range of $1 - 2$ MPa and $w \approx 27$ mJ/mm². The radius of the punch used in all experiments was $R = 27.5$ mm.

We then performed indentation experiments on an adhesive clamped beam and the results are also reported in Fig. 16(b). The beam's half-span $l \approx 50$ mm and thickness $h = 8$ mm. Fig. 16(b) also plots predictions of the theory developed here. For simplic-
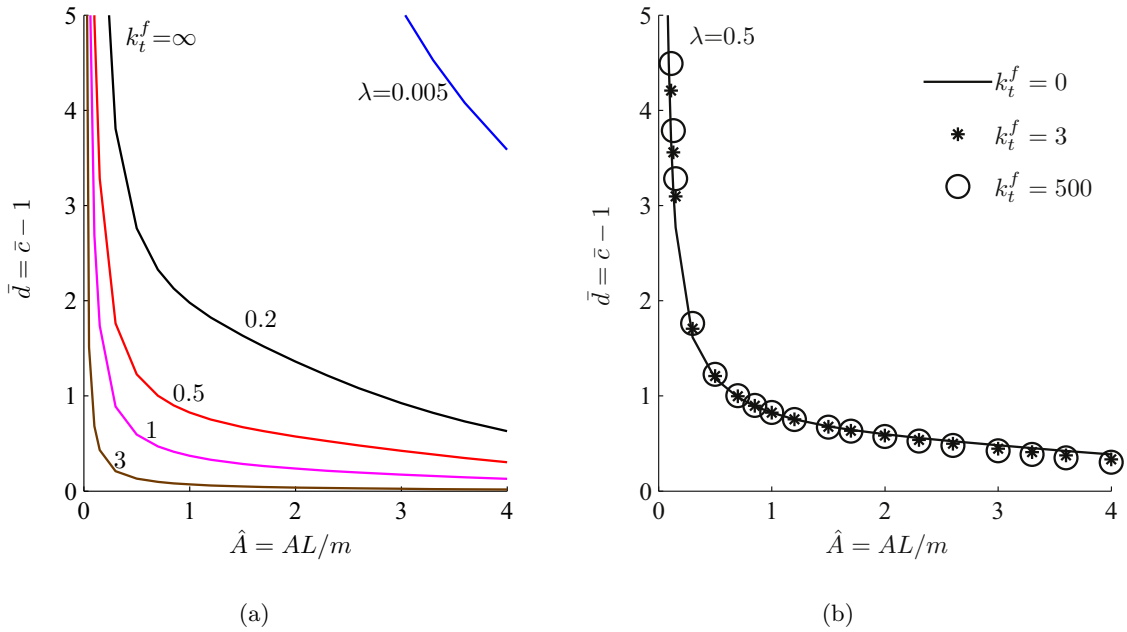
Fig. 15. Adhesive contact of beams on flexible supports with an adhesive zone model. Variation of the adhesive zone's size $\bar{d}$ with the contact area $\hat{A}$ for (a) different adhesive strengths λ, with $k_t^f = \infty$ and $k_s^f = \infty$, and (b) three different torsional spring stiffnesses k_t^f at $\lambda = 0.5$.


Fig. 16. (a) Indentation experiments for an adhesive clamped beam of thickness $h = 8$ mm and half-span $l = 50$ mm. Insets show a closeup of the side view of the indentation and a top view of the contact patch. (b) Variation of the contact area a (in mm) with the total load P (in g). Filled circles represent experimental data. Solid lines correspond to theoretical predictions employing JKR approximation, while the dashed line is for non-adhesive contact. For $h = 8$ mm, we followed Sections 6 and 7, while we employed the standard JKR solution for a half-space when $h = 25$ mm.

ity we restrict ourselves to the JKR approximation of Section 7. We observe from Fig. 16(b) that our theoretical predictions match well with experiments on clamped adhesive beam. From Fig. 16(b) we note that there is significant difference in the contact areas measured during indentation of the beam and for the half-space. Fig. 16(b) also highlights the role of adhesion, as the response for adhesionless contact does not match experiments. These observations underline the importance of modeling the adhesive contact of beams carefully, and in a manner distinct from how we approach indentation of half-spaces.

9.2. Application

Finally, we demonstrate the utility of our semi-analytical procedure to model indentation in structural adhesives with one microchannel, as shown in Fig. 17(a). To generate theoretical predictions, we employ the material and geometric parameters shown in Table 1. The stiffnesses of the flexible end supports are estimated from a strength-of-materials approach to be $k_s^f \approx 12b'l^3/h_ch^3$ and $k_t^f \approx lb'^3/h_ch^3$, where b' is the width of the end supports. Our results are then compared with the experimental results of
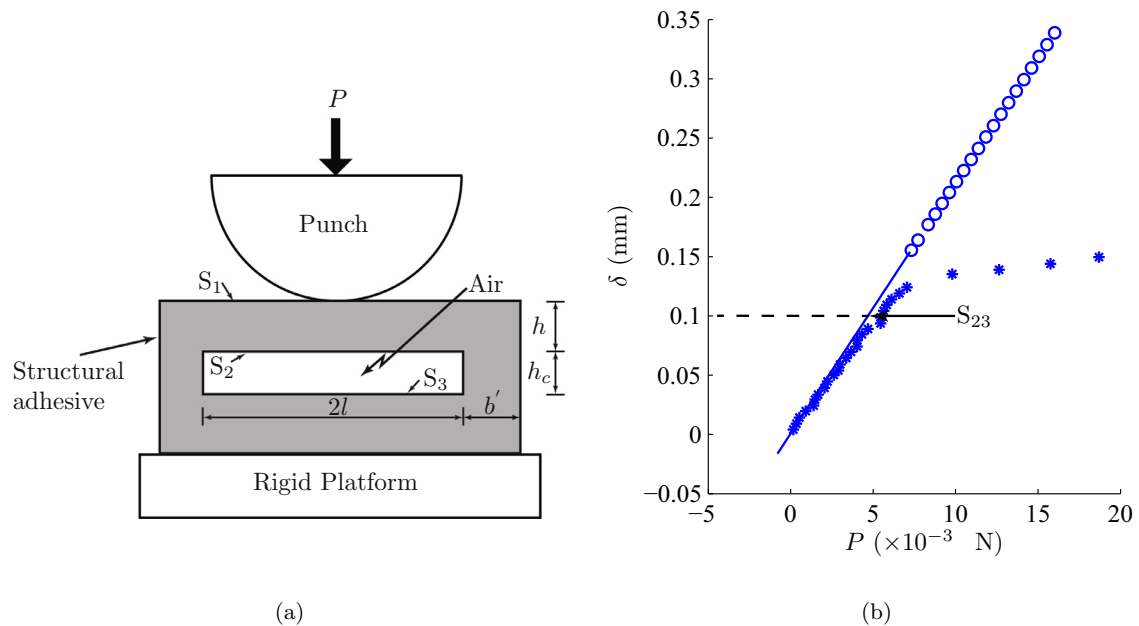
Fig. 17. (a) A structural adhesive with one micro-channel. (b) Variation of the the punch's displacement δ with total load P. The open circles represent the solution for non-adhesive contact obtained from the procedure of Section 6. The solid line represents the solution for adhesive contact obtained from Section 7. Asterisk (*) are the experimental results of Arul and Ghatak (2008).

Table 1
Geometrical and material parameters considered for modeling adhesives with one micro-channel; see also Fig. 17(a). These values are taken from Arul and Ghatak (2008).

Geometrical and material parameters	Value
Beam thickness	$h = 0.8$ mm
Micro-channel's thickness	$h_c = 0.1$ mm
Beam's length	$2l = 5 - 8$ mm
Punch radius	$R = 2.24$ mm
Punch length	$l_p = 2.7$ mm
Shear modulus	$G = 1$ MPa
Poission's ratio	$\nu = 0.49$
Young's modulus	$E = 2(1 + \nu) \approx 3$ MPa
Work of adhesion	$w = 0.045 \times 10^{-3}$ mJ/mm^2 or N/mm

Arul and Ghatak (2008) in Fig. 17(b). We find good agreement upto an indentation depth $\delta \approx 0.1$ mm, i.e. until the point S_{23}. At S_{23}, the surfaces S_2 and S_3 in Fig. 17(a) begins to interact. Currently, we have not consider the interaction between two layers in our mathematical model. Thus, we expect this deviation of our predictions from experiments.

In Fig. 17(b) we reconsider the $\delta - P$ response in the absence of adhesion. Because Arul and Ghatak (2008) did not report measurements of contact area, we assume that the contact area observed is the same as that estimated by the adhesive beam model of the previous paragraph. We note from Fig. 17 that the predictions for adhesionless contact do not match experiments. The slopes, however, do match, as indeed they should be given by Fig. 12(a). This again suggests that experiments should report contact area measurements in addition to total load and displacement.

10. Conclusions

In this article we presented an approximate theoretical model for the indentation of adhesive beams mounted on flexible supports. Adhesion, when present, was incorporated through either the JKR approximation or an adhesive zone model. To simplify and close our mathematical model, we approximated the displacement of the bottom surface of the beam through Euler–Benoulli

beam theory. This was then utilized to formulate a boundary value problem, which is reduced to a single Fredholm integral equation of the first kind for the unknown contact pressure. The integral equation was then solved through a Galerkin projection employing Chebyshev polynomials. Finite element (FE) simulations were carried out for clamped and simply supported non-adhesive beams, and our results compared well with FE predictions, as well as with previously reported theoretical results. Results for adhesive contact were found for several combinations of adhesive strengths, beam geometries, and support flexibilities characterized through torsional and vertical translational springs. Theoretical results for adhesive clamped beam were compared with preliminary experiments and a satisfactory match was observed. Finally, we demonstrated the application of our approach to model a complex structural adhesive.

The semi-analytic technique presented here assumes that the displacement v_b of the beam's bottom surface is approximated well by Euler–Bernoulli beam theory. This assumption is seen to hold for contact areas less than or equal to the beam's thickness, i.e. $a/h \lesssim 1$. For deeper indentations, we need to formulate the contact problem in terms of two unknowns, viz. the contact pressure $p(x)$ and the displacement $v_b(x)$, and then solve the ensuing dual integral equations (Punati, 2017). Investigating adhesive contact of beams experimentally is also useful, and this we are currently pursuing. Looking further forward, we envisage extending our approximate analysis technique to modeling adhesive interaction of one beam with another, as is observed in multi-layered structural adhesives shown in Fig. 1. The present framework may also be adapted to three-dimensional axi-symmetric adhesive contact of punches with plates.

Appendix A. Calculations using beam theory

In this section, we find the displacement of an Euler–Bernouli beam subjected to a point load at its center and resting on flexible supports, as shown in Fig. A.18.

From Euler-Bernoulli beam theory (Crandall et al., 2008, p. 165, 523, 543) we find

$$EI \frac{\mathrm{d}^4 v_n(x)}{\mathrm{d}x^4} = P\langle x\rangle^{-1}, \tag{A.1}$$

where $v_n(x)$ is the displacement of the neutral axis (dash-dot line in Fig. A.18) and

$$\langle x\rangle = \begin{cases} x, & x > 0 \\ 0, & x \leq 0. \end{cases}$$

The appropriate boundary conditions are:

$$v_n|_{x=-l} = \frac{P}{2k_s}, \quad v_n|_{x=l} = \frac{P}{2k_s}, \tag{A.2a}$$

$$k_t \frac{\mathrm{d}v_n}{\mathrm{d}x}\bigg|_{x=-l} = EI\frac{\mathrm{d}^2 v_n}{\mathrm{d}x^2}\bigg|_{x=-l} \quad \text{and} \quad -k_t \frac{\mathrm{d}v_n}{\mathrm{d}x}\bigg|_{x=l} = EI\frac{\mathrm{d}^2 v_n}{\mathrm{d}x^2}\bigg|_{x=l}. \tag{A.2b}$$

Identifying the displacement v_b of the beam's bottom surface with v_n, as is done in beam theory, and solving (A.1) and (A.2), provides

$$v_b(x) = \frac{P}{EI}\left\{\frac{1}{6}\langle x\rangle^3 - \frac{1}{12}x^3 - \frac{x^2 l}{8}\left(1 + \frac{EI}{k_t l + EI}\right)\right.$$
$$\left. + \frac{1}{24}\left(l^3 + 3l^3 \frac{EI}{k_t l + EI} + 12\frac{EI}{k_s}\right)\right\}. \tag{A.3}$$

As the displacement is symmetric in x, we henceforth employ $v_b(x)$ for $x \geq 0$ in our calculations.
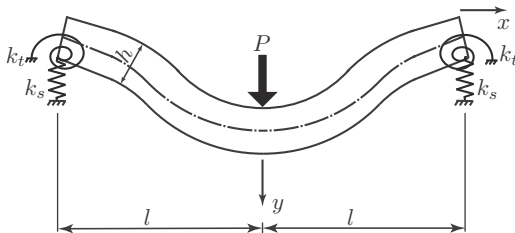
Non-dimensionalizing (A.3) following Section 3, we obtain

$$\vartheta_b(\hat{\tau}) = \frac{4\bar{P}}{3\bar{I}(1-\nu^2)}$$
$$\times \left\{\frac{\langle\hat{\tau}\rangle^3}{6} - \frac{\hat{\tau}^3}{12} - \frac{\hat{\tau}^2}{8}\left(1 + K_t^{-1}\right) + \frac{1}{24}\left(1 + 3K_t^{-1} + 12K_s^{-1}\right)\right\}, \tag{A.4}$$

where $K_t^{-1} = EI/(k_t l + EI) = (1 + k_t^f)^{-1}$ and $K_s^{-1} = EI/k_s l^3 = k_s^{f-1}$.

When we extended the beam to infinity – cf. Fig. 2(b) – the displacement of the overhang, i.e. $\hat{\tau} > 1$, is given by

$$\vartheta_b(\hat{\tau}) = \vartheta_b(\hat{\tau})|_{\hat{\tau}=1} + \frac{\mathrm{d}\vartheta_b(\hat{\tau})}{\mathrm{d}\hat{\tau}}\bigg|_{\hat{\tau}=1}(\hat{\tau} - 1). \tag{A.5}$$

Calculating the displacement and slope at $\hat{\tau} = 1$ from (A.4) and substituting in (A.5) yields

Fig. A.18. An Euler–Bernoulli beam on flexible supports acted upon at its center by a concentrated force P.

$$\vartheta_b(\hat{\tau}) = \frac{4\bar{P}}{3\bar{I}(1-\nu^2)}\left[\frac{1}{2K_s} - \frac{1}{4K_t}(\hat{\tau} - 1)\right], \quad \hat{\tau} > 1. \tag{A.6}$$

Finally, the displacement of the extended beam's bottom surface over its entire length may be written as

$$\vartheta_b(\hat{\tau}) = \frac{4\bar{P}}{3\bar{I}(1-\nu^2)}\vartheta_p(\hat{\tau}), \tag{A.7}$$

where

$$\vartheta_p(\hat{\tau}) = \begin{cases} \left\{\hat{\tau}^3/12 - \hat{\tau}^2(1 + K_t^{-1})/8 + (1 + 3K_t^{-1} + 12K_s^{-1})/24\right\}, \\ \qquad 0 \leq \hat{\tau} \leq 1 \\ \left\{K_s^{-1}/2 - K_t^{-1}(\hat{\tau} - 1)/4\right\}, \quad \hat{\tau} > 1. \end{cases} \tag{A.8}$$

Finally, we evaluate the Fourier transform

$$\hat{\vartheta}_b(\hat{\omega}) = \int_{-\infty}^{\infty}\vartheta_b(\hat{\tau})\cos(\hat{\omega}\hat{\tau})\,\mathrm{d}\hat{\tau} = 2\int_0^{\infty}\vartheta_b(\hat{\tau})\cos(\hat{\omega}\hat{\tau})\,\mathrm{d}\hat{\tau}, \tag{A.9}$$

which is required in (23). The above integrals are typically undefined, as $\vartheta(\hat{\tau})$ is unbounded once the beam is extended to infinity, unless the beam is clamped. To overcome this, we invoke St. Venant's principle by which, displacement of the overhang, sufficiently far away from the supports, may be modified without exerting any significant influence on the displacement and stresses in the portion of the beam lying within the supports. To this end, we modify the displacement of the beam's bottom surface by introducing

$$\vartheta_b^M(\hat{\tau}) = \vartheta_b(\hat{\tau}) \cdot W(\hat{\tau}), \tag{A.10}$$

with

$$W(\hat{\tau}) = \begin{cases} 1, & \text{for } \hat{\tau} \leq \hat{l}_1, \\ w_2(\hat{\tau}), & \text{for } \hat{l}_1 < \hat{\tau} < \hat{l}_2, \\ 0, & \text{for } \hat{\tau} \geq \hat{l}_2 \end{cases} \tag{A.11}$$

where

$$w_2(\hat{\tau}) = \frac{\exp\left\{-1/\left(\hat{l}_2 - \hat{\tau}\right)^2\right\}}{\exp\left\{-1/\left(\hat{l}_2 - \hat{\tau}\right)^2\right\} + \exp\left\{-1/\left(\hat{\tau} - \hat{l}_1\right)^2\right\}}, \tag{A.12}$$

and $\hat{l}_1$ and $\hat{l}_2$ locate points on the beam that are far away from its supports, i.e. $\hat{l}_2 > \hat{l}_1 \gg 1$. The function $W(\hat{\tau})$ is a *mollifier*, see Muthukumar (2016), and is infinitely differentiable everywhere.

The mollified displacement $\vartheta_b^M(\hat{\tau})$ in (A.10) is now utilized in (A.9) to compute the Fourier transforms. Thus,

$$\hat{\vartheta}_b(\hat{\omega}) \approx 2\int_0^{\infty}\vartheta_b^M(\hat{\tau})\cos(\hat{\omega}\hat{\tau})\,\mathrm{d}\hat{\tau}$$
$$= 2\int_0^{\infty}\vartheta_b(\hat{\tau})W(\hat{\tau})\cos(\hat{\omega}\hat{\tau})\,\mathrm{d}\hat{\tau}. \tag{A.13}$$

Evaluating the above integral and replacing the total load $\bar{P}$ from (28) in the resulting equation provides

$$\hat{\vartheta}_b(\hat{\omega}) = \left\{\frac{4\pi b_0}{3\bar{I}(1-\nu^2)} - \frac{4\lambda A m\bar{c}}{3\hat{\gamma}^3\bar{I}L(1-\nu^2)}\right\}\hat{\vartheta}_p(\hat{\omega}), \tag{A.14}$$

where

$$\hat{\vartheta}_p(\hat{\omega}) = 2\int_0^{\infty}\vartheta_p(\hat{\tau})W(\hat{\tau})\cos(\hat{\omega}\hat{\tau})\,\mathrm{d}\hat{\tau}. \tag{A.15}$$

Setting $k_t^f \to \infty$ and $k_s^f \to \infty$, we obtain results for a clamped beam, while those for a simply supported beam are found by taking $k_t^f \to 0$ and $k_s^f \to \infty$.

Finally, we write

$$\frac{1}{\pi\hat{\gamma}}\hat{\vartheta}_b(\hat{\omega}) = \left\{\frac{4b_0}{3\bar{I}(1-\nu^2)\hat{\gamma}} - \frac{4\lambda Am\bar{c}}{3\pi\hat{\gamma}^4\bar{I}L(1-\nu^2)}\right\}\hat{\vartheta}_p(\hat{\omega}). \quad (A.16)$$

Appendix B. Vertical displacement of the beam's top surface in Fourier space $V(\xi, 0)$

In Fourier space, the transformed horizontal and vertical displacements may be solved as, respectively,

$$U(\xi, y) = \{\kappa a_1 + \xi y(a_1 + ia_3)\}e^{\xi y} + \{\kappa b_1 - \xi y(b_1 - ib_3)\}e^{-\xi y}, \quad (B.1)$$

and

$$V(\xi, y) = \{\kappa a_3 + i\xi y(a_1 + ia_3)\}e^{\xi y} + \{\kappa b_3 + i\xi y(b_1 - ib_3)\}e^{-\xi y}, \quad (B.2)$$

with

$$U(\xi, y) = \int_{-\infty}^{\infty} u(x, y)e^{i\xi x}dx \quad \text{and} \quad V(\xi, y) = \int_{-\infty}^{\infty} \nu(x, y)e^{i\xi x}dx,$$

where a_1, a_3, b_1 and b_3 are unknown constants. These constants are obtained by satisfying boundary conditions (2), which in Fourier space are

at $y = 0$: $S_{\xi y} = 0$, $S_{yy} = \bar{P}_c(\xi)$, $\quad (B.3a)$

and at $y = h$: $S_{\xi y} = 0$, $V = \bar{\nu}_b(\xi)$, $\quad (B.3b)$

with

$$S_{\xi y} = \frac{E}{2(1+\nu)}\left(\frac{d}{dy}U - i\xi V\right),$$

$$S_{yy} = \frac{E}{(1+\nu)}\left\{\frac{d}{dy}V + \frac{\nu}{1-2\nu}\left(-i\xi U + \frac{d}{dy}V\right)\right\},$$

$$\bar{P}_c(\xi) = \int_{-\infty}^{\infty} -P_c(x)e^{i\xi x}dx \quad \text{and} \quad \bar{\nu}_b(\xi) = \int_{-\infty}^{\infty} \nu_b(x)e^{i\xi x}dx.$$

Solving (B.1)–(B.3), we obtain the vertical displacement of the beam's top surface in Fourier space as

$$V(\xi, 0) = -\frac{2\bar{P}_c(\xi)}{E^*}\frac{\sinh^2\xi h}{\xi(\xi h + \sinh\xi h\cosh\xi h)}$$

$$+ \bar{\nu}_b(\xi)\frac{\sinh\xi h + \xi h\cosh\xi h}{\xi h + \sinh\xi h\cosh\xi h}.$$

Appendix C. Evaluation of the integrals $\alpha_n(\bar{\omega})$

We recall from (27) in Section 4 that

$$\alpha_n(\bar{\omega}) = \int_{-1}^{1}\frac{1}{\sqrt{(1-\bar{\tau}^2)}}T_n(\bar{\tau})\cos(\bar{\omega}\tau)\,d\bar{\tau}. \quad (C.1)$$

We now compute these integrals explicitly. First, consider odd n. For this, the integrand is an odd function so that

$$\alpha_{2n-1}(\bar{\omega}) = 0. \quad (C.2)$$

Next, evaluating (C.1) for even n we obtain the first few α_n as

$$\alpha_0(\bar{\omega}) = \pi\,J(0, \bar{\omega}),$$

$$\alpha_2(\bar{\omega}) = \pi\,J(0, \bar{\omega}) - \frac{2\pi\,J(1, \bar{\omega})}{\bar{\omega}},$$

$$\alpha_4(\bar{\omega}) = \pi\,J(0, \bar{\omega}) - \frac{8\pi\,J(1, \bar{\omega})}{\bar{\omega}} - \frac{24\pi\,J(0, \bar{\omega})}{\bar{\omega}^2}$$

$$+ \frac{48\pi\,J(1, \bar{\omega})}{\bar{\omega}^3},$$

and

$$\alpha_6(\bar{\omega}) = \pi\,J(0, \bar{\omega}) - \frac{18\pi\,J(1, \bar{\omega})}{\bar{\omega}} - \frac{144\pi\,J(0, \bar{\omega})}{\bar{\omega}^2}$$

$$+ \frac{768\pi\,J(1, \bar{\omega})}{\bar{\omega}^3}$$

$$+ \frac{1920\pi\,J(0, \bar{\omega})}{\bar{\omega}^4} - \frac{3840\pi\,J(1, \bar{\omega})}{\bar{\omega}^5}, \quad (C.3)$$

where $J(n, \bar{\omega})$ are the Bessel's functions of the first kind of order n. Employing the recurrence relation (Polyanin and Manzhirov, 2008, p. 1016),

$$J(n + 1, \bar{\omega}) = \frac{2n}{\bar{\omega}}J(n, \bar{\omega}) - J(n - 1, \bar{\omega}),$$
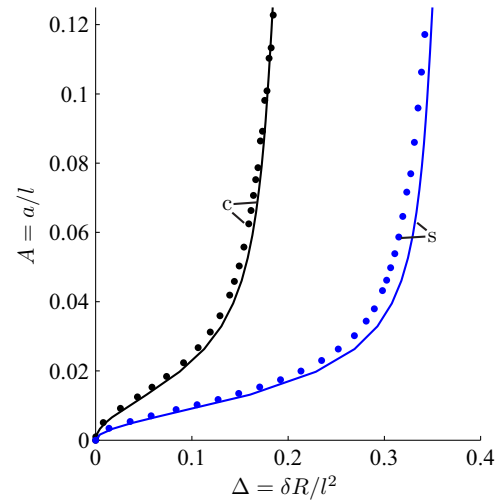
we rewrite (C.3) as

$$\alpha_2(\bar{\omega}) = -\pi\,J(2, \bar{\omega}), \quad \alpha_4(\bar{\omega}) = \pi\,J(4, \bar{\omega})$$

and $\alpha_6(\bar{\omega}) = -\pi\,J(6, \bar{\omega}).$

In general, it is possible to show that

$$\alpha_{2n}(\bar{\omega}) = (-1)^n\pi\,J(2n, \bar{\omega}). \quad (C.4)$$

Appendix D. Additional results

Fig. D.19. Non-adhesive contact of clamped ('c') and simply supported ('s') beams. Variation of the contact area A with the punch's displacement Δ is plotted. The beam's slenderness ratio $l/h=10$. Solid lines are results obtained from the semi-analytical procedure of Section 4. Filled circles correspond to FE simulations of Section 5.
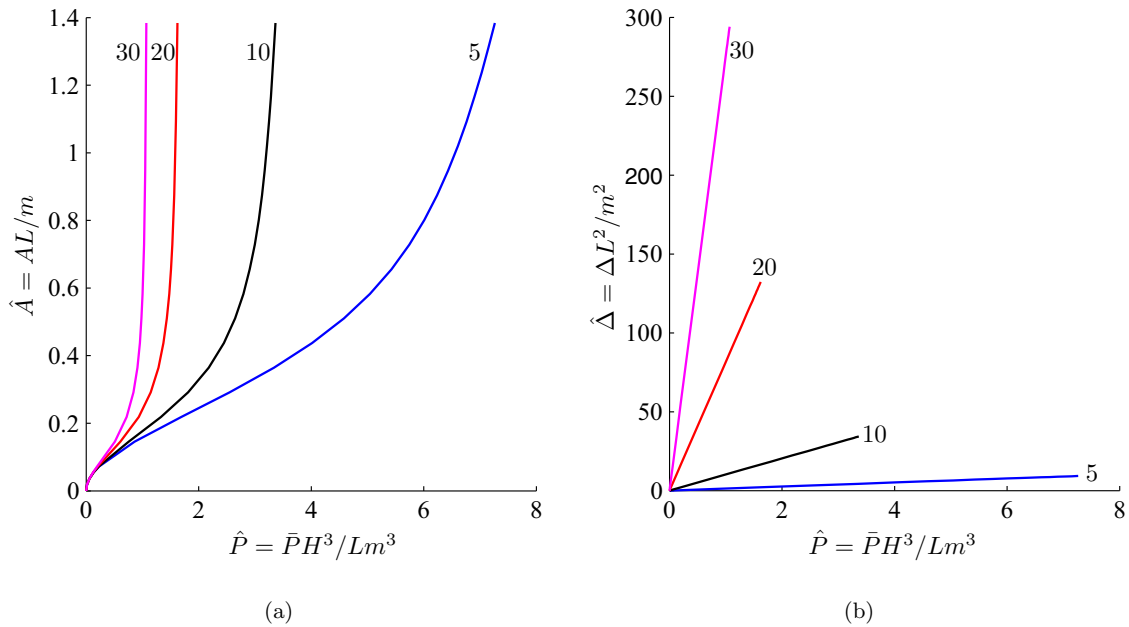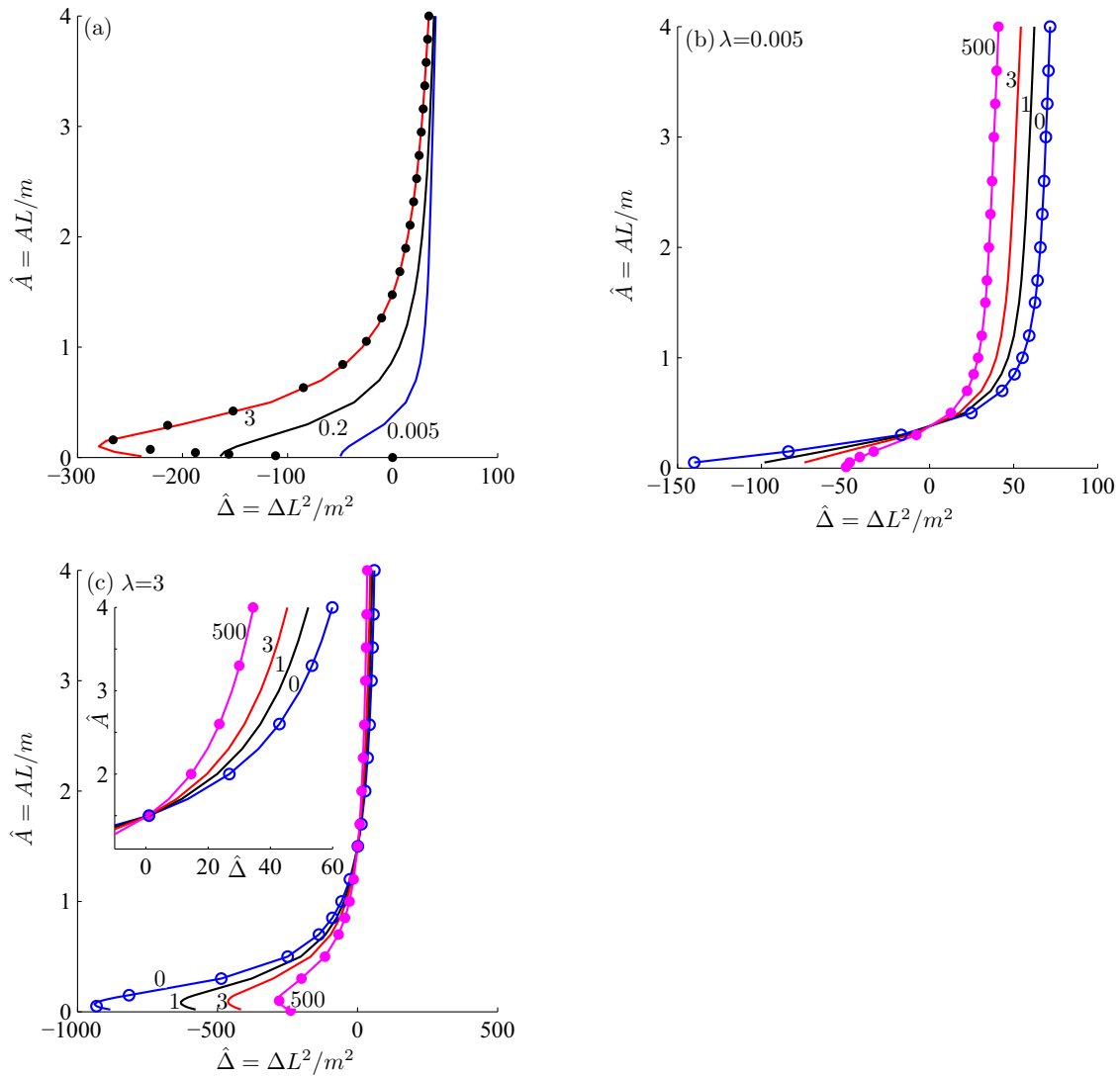
Fig. D.20. Non-adhesive contact of clamped beams. Variation of (a) the contact area $\hat{A}$ and (b) the punch's displacement $\hat{\Delta}$ with total load $\hat{P}$ are shown. Different slenderness ratios l/h are considered and these are noted next to their associated curves.
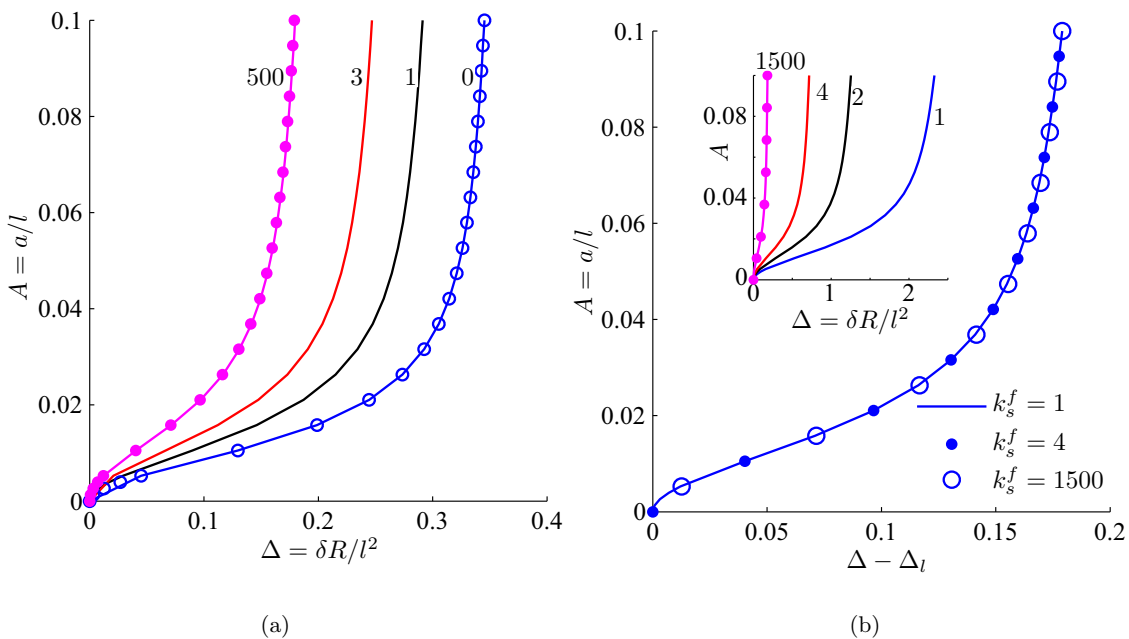
Fig. D.21. Non adhesive contact of beams on flexible supports. The beam's slenderness ratio $l/h = 10$. (a) Variation of contact area A is plotted as a function of the punch's displacement Δ. The vertical translational spring's stiffness $k_s^f = \infty$. Various torsional springs are considered and their stiffnesses k_t^f are indicated next to their associated curves. Open and filled circles represent results for simply supported and a clamped beams, respectively. (b) Variation of contact area A is plotted as a function of the adjusted punch's displacement $\Delta - \Delta_l$ by varying k_s^f. The inset shows the variation of contact area A with the punch's displacement Δ. The torsional spring stiffness $k_t^f = \infty$. Various vertical translational springs are considered and their stiffnesses k_s^f are indicated either in the legend or next to their associated curves. Filled circles in the inset represent results for a clamped beam.
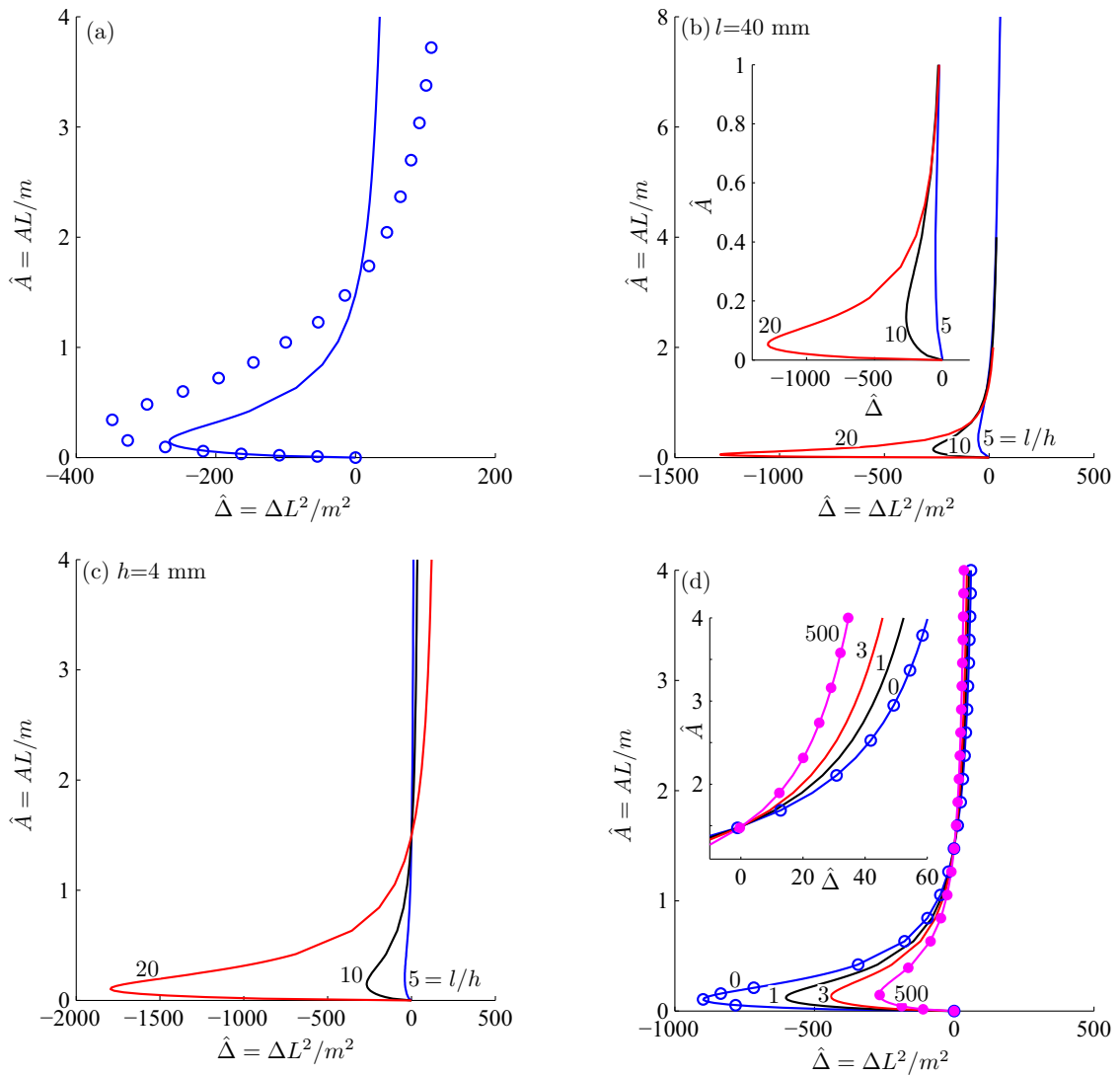
Fig. D.22. Adhesive contact of beams with the JKR approximation. The variation of contact area $\hat{A}$ with the punch's displacement $\hat{\Delta}$ is reported. (a) Two clamped beams are considered with the same slenderness ratio of $l/h = 10$. Solid line correspond to $l = 40$ mm and $h = 4$ mm, while the open circles are for a beam with $l = 80$ mm and $h = 8$ mm. (b) Clamped beams with different slenderness ratio l/h, as shown, are considered. Results are obtained by setting $l = 40$ mm and varying h. (c) Results for clamped beams with different l/h are plotted by setting $h = 4$ mm but different l. In (b) and (c) with increasing l/h the curves move away (outward) from $\hat{\Delta} = 0$ line. (d) A beam with thickness $h = 4$ mm and $l = 40$ mm, which is resting on flexible supports, is considered. The vertical translational spring's stiffness $k_s^f = \infty$. Various torsional springs are considered and their stiffnesses k_t^f are indicated next to their associated curves. The inset correspond to behavior at high $\hat{A}$. Open and filled circles represent results for adhesive beams that are, respectively, simply supported and clamped.

Fig. D.23. Adhesive contact of beams with an adhesive zone model. Variation of the contact area $\hat{A}$ with the punch's displacement $\hat{\Delta}$ is reported. (a) A clamped beam with thickness $h = 4$ mm and $l = 40$ mm is considered. Results are plotted for different adhesive strengths λ as indicated next to their associated curves. Filled circles represent the JKR solution for the corresponding beam; cf. Section 7. (b,c) A beam resting on flexible supports is considered. Beam's thickness $h = 4$ mm and $l = 40$ mm. The vertical translational spring's stiffness $k_s^f = \infty$. Results are plotted for different torsional spring stiffnesses k_t^f as noted next to their associated curves. Two different adhesive strengths λ are considered, as indicated. The inset in (c) depict behavior at high $\hat{A}$. Open and filled circles represent results for a simply supported and a clamped beam, respectively, at the corresponding λ.

References

Alexandrov, A., Pozharskii, D., 2001. Three-Dimensional Contact Problems. Kluwer Academic Publishers, Dordrecht, The Netherlands.

Arul, E.P., Ghatak, A., 2008. Bioinspired design of a hierarchically structured adhesive. Langmuir 25 (1), 611–617.

Barthel, E., Perriot, A., 2007. Adhesive contact to a coated elastic substrate. J. Phys. D: Appl. Phys. 40 (4), 1059–1067.

Chatterjee, A., 2002. Lecture notes: An elementary continuation technique. http://home.iitk.ac.in/~anindya/continuation.pdf.

Chaudhury, M.K., Weaver, T., Hui, C., Kramer, E., 1996. Adhesive contact of cylindrical lens and a flat sheet. J. Appl. Phys. 80 (1), 30–37.

Crandall, S.H., Dahl, N.C., Lardne, T.J., 2008. Mechanics of Solids. Tata McGraw-Hill Education Pvt. Ltd., New Delhi, India.

Dalmeya, R., Sharma, I., Upadhyay, C., Anand, A., 2012. Contact of a rigid cylindrical punch with an adhesive elastic layer. J. Adhes. 88 (1), 1–31.

Galin, L.A., Gladwell, G.M.L., 2008. Contact Problems: The legacy of L.A. Galin. Solid Mechanics and Its Applications. Springer Netherlands.

Gladwell, G.M.L., 1980. Contact Problems in the Classical Theory of Elasticity. Sijthoff & Noordhoff Publishers, Alphen aan den Rijn, The Netherlands.

Hiller, U.J., 1976. Comparative studies on the functional morphology of two gekkonid lizards. Bombay Nat. Hist. Soc. 73, 278–282.

Hills, D.A., Nowell, D., Sackfield, A., 1993. Mechanics of Elastic Contacts. Butterworth-Heinemann, Oxford, UK.

Johnson, K.L., 1985. Contact Mechanics. Cambridge U. Press, Cambridge, UK.

Kanninen, M.F., Popelar, C.L., 1985. Advanced Fracture Mechanics. Oxford U. Press, New York, USA.

Keer, L.M., Miller, G.R., 1983. Smooth indentation of finite layer. J. Eng. Mech. 109 (3), 706–717.

Keer, L.M., Schonberg, W.P., 1986. Smooth indentation of an isotropic cantilever beam. Int. J. Solids Struct. 22 (1), 87–106.

Keer, L.M., Silva, M.A.G., 1970. Bending of a cantilever brought gradually into contact with a cylindrical supporting surface. Int. J. Mech. Sci. 12 (9), 751–760.

Kim, J.H., Ahn, Y.J., Jang, Y.H., Barber, J.R., 2014. Contact problems involving beams. Int. J. Solids Struct. 51 (25–26), 4435–4439.

Mason, J.C., Handscomb, D.C., 2003. Chebyshev Polynomials. Chapman & Hall/CRC, Boca Raton, Florida, USA.

Maugis, D., 1992. Adhesion of spheres: the JKR-DMT transition using a Dugdale model. J. Colloid Interface Sci. 150 (1), 243–269.

Muthukumar, T., 2016. Lecture notes: Sobolev spaces and applications. http://home.iitk.ac.in/~tmk/courses/mth656/main.pdf.

Pandey, A., Moulton, D.E., Vella, D., Holmes, D.P., 2014. Dynamics of snapping beams and jumping poppers. Int. J. Non Linear Mech. 105 (2), 24001.

Plaut, R.H., Virgin., L.N., 2017. Snap-through under unilateral displacement control with constant velocity. Int. J. Non Linear Mech. 94, 292–299.

Polyanin, A., Manzhirov, A., 2008. Handbook of Integral Equations: Second Edition. Chapman & Hall/CRC, Boca Raton, Florida, USA.

Press, W.H., Teukolsky, S.A., Vetterling, W.T., Flannery, P., 1992. Numerical Recipes in C: The Art of Scientific Computing. Cambridge U. Press India Pvt. Ltd., New Delhi, India.

Punati, V.S., 2017. Contact Mechanics of Adhesive Beams. IIT Kanpur Ph.D. thesis.

Rice, J.R., 1968. A path independent integral and the approximate analysis of strain concentration by notches and cracks. J. Appl. Mech. 35 (2), 379–386.

Sadd, M.H., 2005. Elasticity: Theory, Applications, and Numerics. Elsevier India, New Delhi, India.

Sankar, B.V., Sun, C.T., 1983. Indentation of a beam by a rigid cylinder. Int. J. Solids Struct. 19 (4), 293–303.

Sneddon, I.N., 1995. Fourier Transforms. Dover Publications, New York, USA.

Sun, C.T., Sankar, B.V., 1985. Smooth indentation of an initially stressed orthotropic beam. Int. J. Solids Struct. 21 (2), 161–176.

Timoshenko, S.P., Goodier, J.N., 1970. Theory of Elasticity. McGraw-Hill, Singapore.